THE GEOLOGICAL SOCIETY OF AMERICA®

Flow of Devonian anatectic crust in the accretionary Altai Orogenic Belt, central Asia: Insights into horizontal and vertical magma transfer

Sheng Wang[1,2,3], Yingde Jiang[1,2,†], Roberto Weinberg[4], Karel Schulmann[5,6], Jian Zhang[7], Pengfei Li[1,2], Ming Xiao[1,2], and Xiao-Ping Xia[1,2]

[1]*State Key Laboratory of Isotope Geochemistry, Guangzhou Institute of Geochemistry, Chinese Academy of Sciences, Guangzhou 510640, China*
[2]*CAS Center for Excellence in Deep Earth Science, Guangzhou, 510640, China*
[3]*University of Chinese Academy of Sciences, Beijing 100049, China*
[4]*School of Earth, Atmosphere and Environment, Monash University, Clayton, Victoria 3800, Australia*
[5]*Czech Geological Survey, Centre for Lithospheric Research, Klárov 3, 118 21 Praha 1, Czech Republic*
[6]*Université de Strasbourg, CNRS, IPGS UMR 7063, Strasbourg F-67000, France*
[7]*School of Earth Sciences and Engineering, Sun Yat-sen University, Guangzhou 510275, China*

ABSTRACT

Flow of partially molten crust is a key contributor to mass and heat redistribution within orogenic systems, however, this process has not yet been fully understood in accretionary orogens. This issue is addressed in a Devonian migmatite-granite complex from the Chinese Altai through structural, petrological, and geochronological investigations presented in this study. The migmatite-granite complex records a gradual evolution from metatexite, diatexite to granite and preserves a record of two main Devonian phases of deformation designated D1 and D2. The D1 phase was subdivided into an early crustal thickening episode ($D1_B$) and a later extensional episode ($D1_M$) followed by D2 upright folding. The $D1_M$ episode is associated with anatexis in the deep crust. Vertical shortening, associated with $D1_M$, gave rise to the segregation of melt and formation of a sub-horizontal layering of stromatic metatexite. This fabric was reworked by the D2 deformation associated with the migration of anatectic magma in the cores of F2 antiforms. Geochronological investigations combined with petro-structural analysis reveal that: (1) $D1_M$ partial melting started probably at 420–410 Ma and formed sub-horizontal stromatic metatexites at ~30 km depth; (2) The anatectic magma accumulated and migrated when a drainage network developed, as attested by the pervasive formation of massive diatexite migmatites, at 410–400 Ma; (3) Soon after, massive flow of the partially molten crust from orogenic lower to orogenic upper crustal levels, assisted by the interplay between D2 upright folding and magma diapirism, led to migmatite-granite emplacement in the cores of regional F2 antiforms that lasted until at least 390 Ma; (4) a terminal stage was manifested by the emplacement of 370–360 Ma granite dykes into the surrounding metamorphic envelope. We propose that Devonian anatexis assisted by deformation governed first the horizontal and then the vertical flow of partially molten orogenic lower crust, which drove crustal flow, mass redistribution, and crustal differentiation in the accretionary system of the Chinese Altai.

1. INTRODUCTION

Exposed orogenic roots are commonly characterized by the presence of migmatites and associated granitic plutons, attesting to considerable crustal anatexis (Whitney et al., 2004; Brown, 2010; Weinberg et al., 2018). Crustal anatexis plays an important role in the evolution of orogens because it strongly influences the thermal and rheological behavior of orogenic crust. It has been shown that the presence of even a low volume of melt (~7 vol%) can significantly decrease rock strength (Rutter and Neumann, 1995; Rosenberg and Handy, 2005; Závada et al., 2007), which can form mechanically weak zones in the crust responsible for lateral displacements (Kruckenberg et al., 2011; Betka and Klepeis, 2013; Whitney et al., 2013). In regions of continental collision, the over-thickened crust is generally associated with intense ductile deformation and extensive partial melting at deep crustal levels (e.g., Vanderhaeghe et al., 2003). The presence of this hot, partially molten material in the deep crust has been imaged by geophysical surveys in a number of modern mountain belts, notably the Himalayan-Tibetan system (e.g., Nelson et al., 1996; Unsworth et al., 2005). Here, crustal flow is in response to gravity or tectonic stresses on scales of tens to hundreds of kilometers (Clark and Royden, 2000; Royden et al., 2008; Brown, 2010; Jamieson et al., 2011).

Collisional orogens can form thickened orogenic root systems where continental crust can reach 70 km thick or more (e.g., Le Pichon et al., 1997). In contrast, accretionary orogens are characterized by moderate or negligible thickening as demonstrated, for instance, by the Ryoke Belt in southwest Japan (Uyeda and Miyashiro, 1974; Skrzypek et al., 2016). Consequently, crustal melting in collisional orogens is commonly associated with contemporaneous ultra-high pressure metamorphism (e.g., Zhang et al., 2010; Labrousse et al., 2015; Štípská et al., 2019; Závada et al., 2018), whereas in accretionary orogens melting tends to develop during low-pressure/high-temperature metamorphism (Collins, 2002; Hyndman et al., 2005; Brown, 2010). Given that accretionary orogens commonly contain abundant fertile components, crustal anatexis can produce a large amount of melt that influences the rheology of the lower crust and thermal budget of the whole orogen (Collins and Richards, 2008; Brown, 2009; Weinberg et al., 2013; Weinberg et al., 2018). However, our knowledge of crustal flow in hot and partially molten accretionary orogens remains fragmental (e.g., Lehmann et al., 2017).

Yingde Jiang https://orcid.org/0000-0002-9533-0146

†Corresponding author: jiangyd@gig.ac.cn.

GSA Bulletin; November/December 2021; v. 133; no. 11/12; p. 2501–2523; https://doi.org/10.1130/B35645.1; 15 figures; 1 supplemental file.
published online 16 March 2021

Migmatite-granite complexes, representing exhumed anatectic orogenic lower crust, highlight the important interplay between crustal melting and deep crust flow during orogenesis (Whitney et al., 2004). Migmatite-granite complexes have been increasingly recorded in accretionary orogenic systems and carry important clues regarding both horizontal and vertical movements of partially molten crust (Norlander et al., 2002; Gervais et al., 2010; Broussolle et al., 2015; Jiang et al., 2015, 2019; Zhang et al., 2015). In this contribution, we focus on a typical migmatite-granite complex in the Chinese Altai that represents one of many high-grade cores of the Central Asian Orogenic Belt (CAOB, also called the Altaids or the Altaid Collage) (Fig. 1A). The Chinese Altai was originally a segment of a huge Late Cambrian–Ordovician sedimentary accretionary wedge formed during the long-lasting retreat of the Paleo-Pacific subduction system (Jiang et al., 2017). It was strongly reworked during the Devonian orogenic event (420−360 Ma), which led to widespread crustal anatexis and magmatism forming granulite-facies orogenic lower crust (Cai et al., 2011b; Jiang et al., 2016, 2019). This orogenic lower crust is exposed in cores of migmatite-granite complexes alternating with lower grade metasedimentary sequences in both Chinese and Mongolian parts of the Altai Range (Broussolle et al., 2015; Jiang et al., 2016). These complexes offer an excellent natural laboratory to study the relationships between melt transfer and deformation (e.g., Lehmann et al., 2017).

In this study, the process of flow of anatectic lower crust is examined by investigating the structural, metamorphic, and temporal evolution of a typical migmatite-granite complex and its metamorphic envelope in the western Chinese Altai. Here, high-precision geochronological constraints on the timing and duration of crustal anatexis and deformation are provided by zircon U-Pb dating of selected migmatites and granitic rocks. Our results reveal that Devonian anataxis, assisted by deformation, governed first the horizontal and then the vertical flow of the partially molten orogenic lower crust. This process led to mass and heat redistribution in the partially molten accretionary wedge and its transformation into a mature continent crust.

2. GEOLOGICAL FRAMEWORK

As the world's largest accretionary system, the CAOB extends from the Ural Mountains to the west to the Pacific Ocean to the east and from the Siberian Craton to the north to the North China and Tarim Craton to the south (Fig. 1A). This giant accretionary system is characterized by a long-lived accretionary process that lasted from the Neoproterozoic to late Paleozoic (Şengör et al., 1993; Windley et al., 2007; Wilhem et al., 2012). Such a prolonged accretion process involved the amalgamation of different geological units and oroclinal bending, thus generating complicated patterns of magmatism, metamorphism, and deformation (e.g., Lehmann et al., 2010; Xiao et al., 2015). The main geological units that constitute the CAOB include Precambrian continental fragments, Paleozoic arcs, ophiolites, accretionary wedges, and arc-related basins (Coleman, 1989; Buslov et al., 2004; Xiao et al., 2009, 2015). Xiao et al. (2015) proposed that the CAOB could be subdivided into three main collage systems: the Mongolian Collage in the east, the Kazakhstan Collage in the west, and the Tarim-North China Collage in the south (Fig. 1A). The Mongolian Collage is centered on Precambrian micro-continental blocks (namely Tuva-Mongolia, Zabkhan, and Baydrag) overthrusted by late Proterozoic ophiolites and accretionary wedges during an Early Cambrian accretionary event (Štípská et al., 2010; Buriánek et al., 2017; Jiang et al., 2017). This event was followed by long-lasting subduction of oceanic crust which gave rise to the generation of the ~1800-km-long Cambro-Ordovician Ikh-Mongol arc system forming a rim at the western margin of the Precambrian micro-continental blocks (Fig. 1B, Janoušek et al., 2018). Meanwhile, a coeval ~2500-km-long volcano-sedimentary unit, formed the Altai accretionary wedge, developed along the margin of the arc system (Fig. 1B) (Jiang et al., 2017; Soejono et al., 2018). The Altai accretionary wedge was subsequently reworked during the Devonian–Carboniferous, leading to significant crustal anatexis and magmatism, clustered at 420−360 Ma (Demoux et al., 2009; Cai et al., 2011b; Hanžl et al., 2016; Jiang et al., 2016). This widespread anatexis also resulted in the formation of a large number of Paleozoic high-grade metamorphic domains cored by partially molten migmatite-granite complexes, typically developed in the southern margin of the Altai Range (Broussolle et al., 2015; Jiang et al., 2015; Hanžl et al., 2016; Lehmann et al., 2017).

The Chinese segment of the Altai wedge, namely the Chinese Altai is separated to the south from the Devonian–Carboniferous Junggar arc domain by the NW-trending Erqis Fault (Fig. 1C) (Li et al., 2015a, 2015b; Xiao et al., 2009). The Chinese Altai is characterized by exhumed migmatite-granite complexes alternating with a low-to-medium-grade metamorphic Ordovician and Devonian sedimentary sequence (Zhuang, 1994; Jiang et al., 2015, 2016; Zhang et al., 2015; Broussolle et al., 2019; Jiang et al., 2019) (Fig. 1C). The Ordovician sedimentary sequence, named the Habahe Group, is the oldest and most widely distributed sedimentary sequence. It experienced intense and multiple deformation events and greenschist- to amphibolite-facies metamorphism, forming schists and gneisses (Long et al., 2008; Sun et al., 2008). The protolith of the Habahe Group mainly consists of quartzo-feldspathic clastic turbidites and pyroclastic rocks (Long et al., 2008; Jiang et al., 2011). These rocks were previously considered to represent passive margin sediments (Chen and Jahn, 2002), but recently published geochemical data have indicated that they are compositionally similar to greywacke and have been reinterpreted as active margin sediments (Long et al., 2008). This is supported by the fact that more than 70% of the detrital zircons from the Habahe Group have positive zircon $\varepsilon_{Hf}(t)$ values, suggesting that the metasedimentary rocks contain abundant young and geochemically primitive components (Cai et al., 2011a).

The Devonian sedimentary sequence consists of weakly metamorphosed volcanic and pyroclastic rocks (Broussolle et al., 2019; Jiang et al., 2019). Some Devonian volcanic rock sequences have bimodal geochemical characteristics and are thought to have been generated in an extensional environment either due to back-arc spreading (Xu et al., 2003; Wan et al., 2011) or associated with retreat of the Paleo-Pacific subduction system (Jiang et al., 2019; Li et al., 2019; Cui et al., 2020).

2.1. Overview of the Devonian Deformation, Metamorphism, and Magmatism

The Altai accretionary wedge was transformed into a mature orogenic belt during a Devonian orogeny as manifested by multiple phases of deformation, regional-scale metamorphism, and widespread intrusion of Circum-Pacific S-type granites (Qu and Zhang, 1994; Wang et al., 2006; Wei et al., 2007; Cai et al., 2011b; Jiang et al., 2015, 2016, 2019; Li et al., 2017). As a consequence, the crust of the Chinese Altai represents a vertically layered edifice broadly formed by granulitized and partially molten Habahe Group rocks in the deep crust, greenschist- to amphibolite-facies metamorphosed but un-molten Habahe Group in the middle, and a non- to weakly metamorphosed Devonian volcanoclastic succession in the upper crust (e.g., Broussolle et al., 2018). Jiang et al. (2019) further defined these three rock packages as orogenic lower crust roughly 25–35 km depth, orogenic middle crust 8–25 km depth, and orogenic upper crust 0–8 km depth (see details in fig. 15A of Jiang et al., 2019). However, this layered crustal structure does not correspond to the geophysical subdivisions of continental crust into a mafic lower, an intermediate middle, and

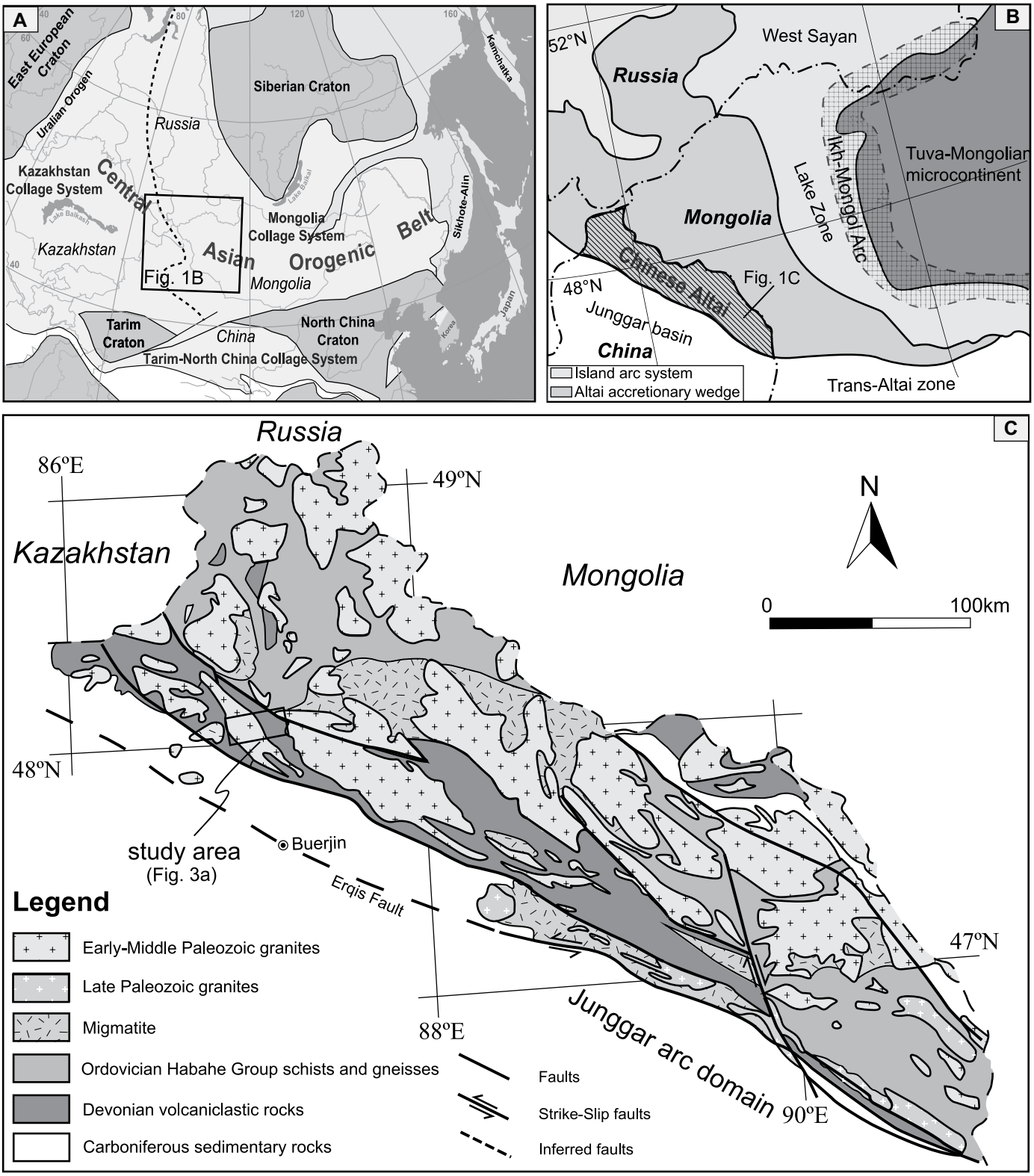

Figure 1. (A) Geological map showing tectonic location of the Central Asian Orogenic Belt (modified after Windley and Xiao, 2018). Extents of the Mongolian Collage System, the Kazakhstan Collage System, and the Tarim-North China Collage System are indicated. The inferred contact between the Mongolian and Kazakhstan collage systems is indicated by a dashed line. (B) A simplified geological map showing major tectono-lithological units of the Mongolian Collage System and the location of the Chinese Altai (modified after Jiang et al., 2017). Extent of the Ikh-Mongol arc system is outlined. (C) Geological map of the Chinese Altai showing main lithological units (modified after Jiang et al., 2016).

a felsic upper crust (Christensen and Mooney, 1995), but it reflects the degree of metamorphic and magmatic differentiation of an originally lithologically homogeneous accretionary wedge (Guy et al., 2020). This primary, vertically stratified crust was affected by two orthogonal important regional-scale folding events during the Mid-to-Late Devonian and Early Permian, respectively (Jiang et al., 2015, 2019; Zhang et al., 2015; Broussolle et al., 2019). The Devonian folding reflects tectonic switching from extension to shortening under a supra-subduction regime, while the Permian folding marks the collision between the Chinese Altai and the Junggar domain to the south (Fig. 1) (Li et al., 2017; Jiang et al., 2019; Zhang et al., 2018a, 2018b). In the following sections, we summarize the published structural, petrological, and geochronological aspects of the Devonian events in the Chinese Altai.

2.1.1. Structural Evolution

An ubiquitous sub-horizontal metamorphic foliation developed in both the un-molten and molten Habahe Group, which was taken as the oldest metamorphic fabric in the region (Broussolle et al., 2019; Jiang et al., 2019). Recent studies suggested that the foliation developed in un-molten and molten Habahe Group rocks reflect distinct tectono-thermal events, despite both being sub-horizontal (Jiang et al., 2019). The foliation in the un-molten Habahe Group is associated with recumbent isoclinal folding (Jiang et al., 2015; Zhang et al., 2015) and contains typical Barrovian-type staurolite- and/or kyanite-bearing assemblages (Jiang et al., 2019). In contrast, the foliation in the migmatitic Habahe Group rocks is commonly associated with extensional lock-up shear bands filled with granitic leucosomes and contains typical high-temperature/low-pressure (HT/LP) garnet-sillimanite-K-feldspar-cordierite assemblages (Jiang et al., 2015, 2019). These differences led Jiang et al. (2019) to divide S1 into a horizontal $S1_B$ foliation and a horizontal $S1_M$ one in un-molten and migmatitic Habahe Group rocks, respectively. Notably, the $S1_M$ in the molten Habahe Group rocks contains $S1_B$ staurolite-kyanite relicts (Jiang et al., 2015), implying that the $S1_M$ overprinted the $S1_B$. These petro-structures together with their metamorphic pressure-temperature evolution, led Jiang et al. (2015) to suggest that the $D1_B$ phase of deformation is commonly considered to be a consequence of crustal shortening associated with pre-Early Devonian accretion, which led to the burial and thickening of the crust. In contrast, the $D1_M$ phase of deformation is considered to be a result of crustal extension which gave rise to the formation of horizontal granite sheets in the orogenic lower crust and extensional-related volcanic basins with bimodal geochemical volcanic rocks in the orogenic upper crust (e.g., Xu et al., 2003; Wan et al., 2011; Jiang et al., 2016, 2019). The timing of the $D1_B$ crustal shortening has so far not been well-constrained while that of the $D1_M$ crustal extension is constrained by the zircon U-Pb ages of granites associated with melt-present extensional shear bands in the partially molten lower crust and by overlying rhyolite in the Devonian extensional basins, as those in southern Chinese Altai (eg., Chai et al., 2009; Guo et al., 2015), all of which yielded 400–380 Ma ages (Zhang et al., 2015; Broussolle et al., 2018; Jiang et al., 2019).

The subsequent main phase of deformation (designated D2) is related to a crustal-scale shortening that gave rise to numerous NW-SE–trending upright F2 folds in the region. This event has variable expressions at different crustal levels. In the orogenic lower crust, D2 folding resulted in significant transposition of early fabrics and formation of a new sub-vertical migmatitic-magmatic foliation (S2), implying high-temperature conditions (Jiang et al., 2015, 2019; Zhang et al., 2015). In the orogenic middle and upper crust, the pre-existing metamorphic foliation ($S1_B$) as well as sedimentary bedding (S0) were rotated to upright or moderately dipping positions with local transposition into the new S2 foliation (e.g., Broussolle et al., 2018; Jiang et al., 2019). The D2 deformation was also responsible for the juxtaposition of the orogenic lower crust with the orogenic middle and upper crust, as exemplified by the fact that migmatite-granite complexes (the anatectic section of the Habahe Group) closely alternate with the lower-metamorphic grade un-molten Habahe Group and the Devonian metasedimentary sequence in the region (e.g., Jiang et al., 2016). There are no specific age constraints for the D2 upright folding, but it likely took place soon after the $D1_M$ extension since the exhumation of the migmatites in the core of F2 antiforms is associated with the presence of magmas (Jiang et al., 2019).

2.1.2. Metamorphic History

The Devonian metamorphic evolution of the Chinese Altai is characterized by the replacement of a typical middle-temperature/middle-pressure (MT/MP) Barrovian-type metamorphic series by a HT/LP series (Jiang et al., 2015). The Barrovian-type metamorphic series is marked by the formation of sub-horizontal metamorphic isograds from structurally shallow chlorite-biotite zone through garnet, staurolite zones to structurally deep kyanite and sillimanite zones (Jiang et al., 2019). This metamorphic fabric was considered synchronous with the first thickening phase $D1_B$ (see section 2.1.1, Jiang et al., 2015). The maximum pressure condition is recorded in the kyanite-sillimanite zone, which has a *P*-max of 8 kbar, corresponding to burial to a depth of ~30 km (Fig. 2, Wei et al., 2007; Jiang et al., 2015). The burial history is thought to have developed during Late Silurian or Early Devonian, at least, predating the 400 Ma granites that crosscut the Barrovian-type metamorphic isograds (Jiang et al., 2019). The prominent Devonian metamorphic phase in the Chinese Altai is a HT/LP metamorphism marked by the extensive crustal anatexis in the lower crust, where the pre-existing Barrovian-type metamorphic series re-equilibrated at higher temperatures (~750 °C/7 kbar) and resulted in garnet-K-feldspar granulite-facies overprint (Fig. 2B, see also Jiang et al., 2015, 2019). Phase equilibrium modeling suggests that this high-temperature metamorphism was connected with either isobaric heating or heating associated with moderate pressure decrease (Fig. 2B, Jiang et al., 2019). This event was considered to be related to the $D1_M$ extension (Broussolle et al., 2019; Jiang et al., 2019). The timing of the high-temperature metamorphic overprint was constrained by U-Pb dating of metamorphic zircon rims in migmatites (400−390 Ma, Jiang et al., 2010). The sub-horizontal metamorphic isograds were subsequently rotated to a near vertical position during D2 upright folding (Jiang et al., 2015, 2019; Zhang et al., 2015). During this process, peak assemblages in most Barrovian-type metamorphic zones were rarely re-equilibrated, probably due to the absence of aqueous fluids (Wei et al., 2007; Jiang et al., 2015). However, in the orogenic lower crust, the peak assemblages were re-equilibrated with melt during D2 as testified by the occurrence of cordierite-bearing low-pressure assemblages in the exhumed migmatites (Fig. 2B, Jiang et al., 2019).

2.1.3. Granites

The Chinese Altai is intruded by large volumes of Devonian granites with U-Pb zircon crystallization ages varying from 420 to 370 Ma, peaking at 400−389 Ma (Cai et al., 2011b). They are mainly two-mica granites with minor hornblende granodiorites (Wang et al., 2006; Yuan et al., 2007; Sun et al., 2008). Devonian granitic rocks commonly show arc-type geochemical affinities with metaluminous to peraluminous compositions (Wang et al., 2006; Yuan et al., 2007; Sun et al., 2008; Cai et al., 2011a). They are thought to be derived from an arc-related magmatic source, on account of their apparent subduction-related geochemical characteristics (Wang et al., 2006; Yuan et al., 2007; Cai et al., 2011b). However, these granites are compositionally comparable to melts derived from partial melting of the Ordovician Habahe Group (Liu et al., 2012; Jiang et al., 2016; Huang

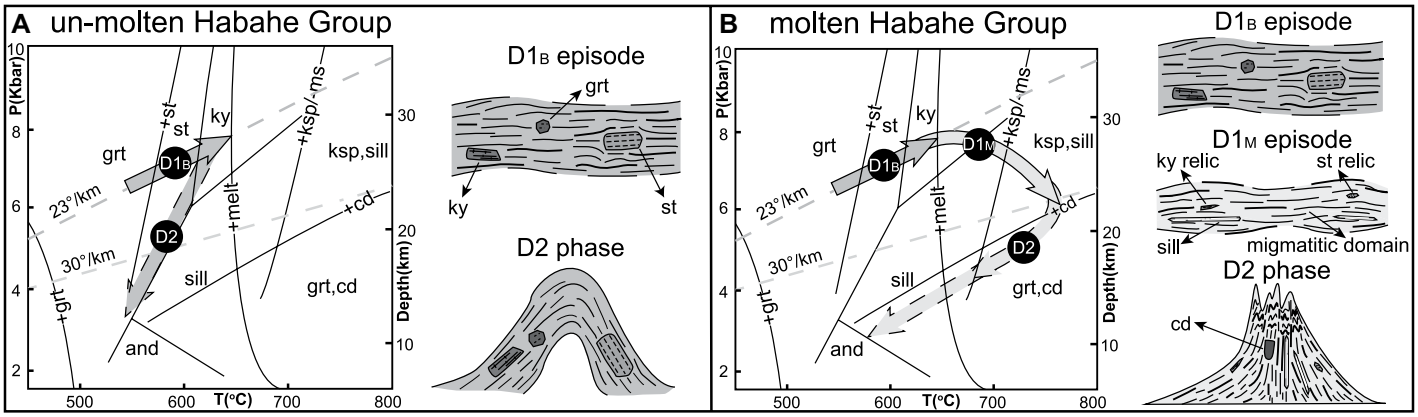

Figure 2. Qualitative pressure (P)-temperature (T) paths for (A) the un-molten Habahe Group (metamorphic envelope) and (B) the molten Habahe Group (migmatites) metasedimentary rock sequence in the Chinese Altai, central Asia. Prograde paths are deduced from the crystallization of the mineral succession in the kyanite and garnet-cordierite zones (Data source from Jiang et al., 2015, 2019; Wei et al., 2007; Broussolle et al., 2019). Insert sketches show the deformational-metamorphic evolution of un-molten/molten Habahe Group rocks at different evolution stages. Note that both molten and un-molten Habahe Group rocks shared a $D1_B$ episode of deformation generating Barrovian-type metamorphic mineral assemblages. The molten Habahe Group experienced an advanced episode of deformation ($D1_M$) forming a migmatitic domain in the orogenic lower crust associated with development of sillimanite-bearing high-temperature foliation $S1_M$. Finally, both molten and un-molten Habahe Group rocks were affected by regional F2 upright folding. Mineral abbreviations: cd—cordierite; grt—garnet; ky—kyanite; sill—sillimanite; st—staurolite; ksp—K-feldspar; ms—muscovite. See text for details.

et al., 2020b). Moreover, these granites show close temporal and spatial relationships with the anatexis of the Habahe Group, as well as their geochemical similarities (Jiang et al., 2016; Huang et al., 2020a). Therefore, these authors suggested that the majority of Devonian granites in the Chinese Altai could be explained by magmatic recycling of the chemically primitive Habahe Group during $D1_M$ crustal extension.

2.2. Overview of Permian Tectono-Thermal Evolution

Compared to the Devonian tectono-thermal events, the Permian ones are less extensive. Permian structures are mainly restricted to the southern Chinese Altai, as exemplified by SSW-ward thrust systems as well as tight upright folding associated with the development of penetrative WNW-ESE–trending schistosity defining an S3 foliation (Qu and Zhang, 1994; Briggs et al., 2007, 2009; Zhang et al., 2012, 2015; Li et al., 2015a, 2016, 2017; Broussolle et al., 2018; Hu et al., 2020). A coeval regional-scale, orogen-parallel, strike-slip displacement also developed at this time, as exemplified by the formation of the ~2000 km WNW-striking Erqis Fault (Fig. 1C, see also Laurent-Charvet et al., 2003). Associated with the Permian deformation, migmatites and granulites were extruded forming km- to dozens of km-wide high-temperature zones along the southern margin of the Chinese Altai (e.g., Broussolle et al., 2018). These rocks are characterized by low-pressure/(ultra) high-temperature metamorphic assemblages and contain abundant Permian metamorphic zircon and monazite U-Pb ages ranging from 290 to 260 Ma (Briggs et al., 2007; Wang et al., 2009; Li et al., 2014; Tong et al., 2014; Liu et al., 2020). Coeval magmatism is expressed by volumetrically small late Paleozoic A-type granitoids or gabbroic bodies dated at 300–270 Ma (Wang et al., 2009; Zhang et al., 2014). These polyphase tectono-thermal events are commonly interpreted as an overall response to the amalgamation between the Chinese Altai and the southerly Junggar arc domain (Li et al., 2016, 2017; Jiang et al., 2019).

2.3. Geology of the Study Area

This study focuses on the Tarlang metamorphic massif, north of Buerjin city, in the western Chinese Altai (Figs. 1C and 3). The massif is ~10 km wide and composed mainly of a composite migmatite-granite complex and a metamorphic envelope formed by metamorphosed but un-molten Habahe Group rocks (Fig. 3) (Jiang et al., 2015; Zhang et al., 2015). The complex mainly consists of granites and migmatitic gneisses with rare amphibolites. The granites are essentially two-mica granites, some with schlieren-rich structures. The migmatitic gneisses are mainly composed of stromatitic to nebulitic rocks that represent the partially molten Habahe Group rocks (Sun et al., 2008). There is a gradual decrease in leucosome proportions from the migmatite-granite complex in the core toward its un-molten envelope (Fig. 3). A weakly to non-metamorphosed volcanic to volcanoclastic succession unconformably overlies the Habahe Group (Fig. 3, Jiang et al., 2015). Zircons from felsic volcanic rocks of this succession yielded Early-Middle Devonian ages of eruption (Zhang et al., 2000; Chai et al., 2009; Liu et al., 2010; Zhang et al., 2015).

The study area records sub-horizontal, geometrically parallel, foliations in both the un-molten Habahe Group rocks and the migmatite-granite complex. The foliation in the former is composed of MT/MP Barrovian-type assemblages and that in the latter consists of HT/LP metamorphic assemblages (Jiang et al., 2015). Here, we use terms $S1_B$ and $S1_M$ for the foliations in un-molten and molten Habahe Group rocks, respectively, in accordance with the previous study of Jiang et al., (2019). The $S1_M$ in the migmatite-granite complex was dated at Middle Devonian (Jiang et al., 2010), whereas the precise formation age of $S1_B$ has so far been undetermined. Previous petro-structural analysis illustrated that the $S1_M$ contained a garnet-sillimanite-K-feldspar-bearing mineral assemblage with modeled peak temperature-pressure conditions of ~800 °C/7 kbar (Jiang et al., 2015). Structural restorations further interpreted that the $S1_M$ was a consequence of sub-vertical shortening associated with orogen-parallel crustal extension ($D1_M$, Jiang et al., 2015; Zhang et al., 2015). Inclusions of staurolite and kyanite preserved in zoned garnet in same migmatite are compatible with an earlier prograde Barrovian pressure-temperature path evolving from the staurolite-stability field (~600 °C/6 kbar) to the kyanite-stability field (~700 °C/8 kbar, Jiang

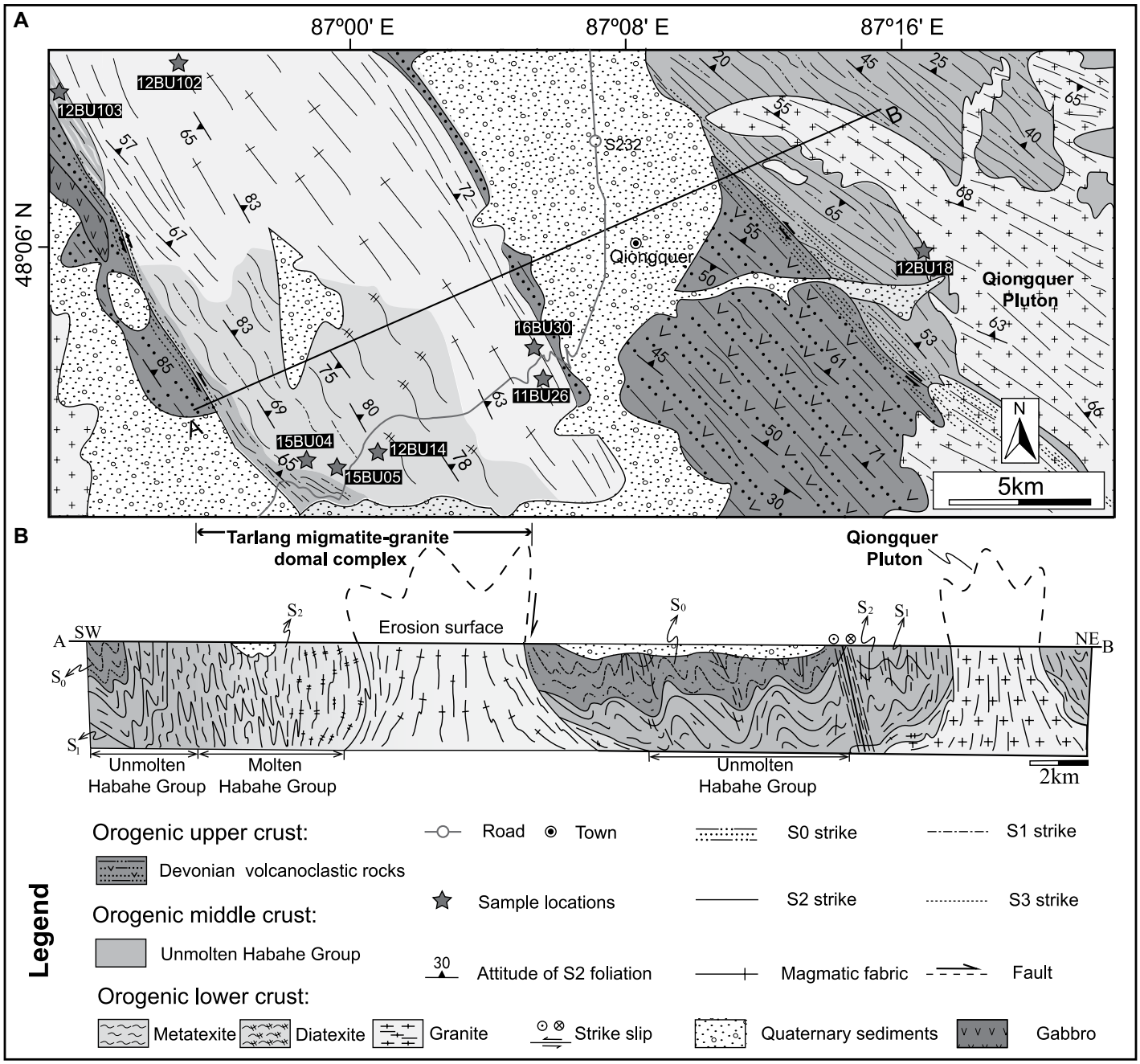

Figure 3. (A) Geological map of the study area (western Chinese Altai, see position in Fig. 1C) showing the Tarlang migmatite-granite complex and its metamorphic envelope. The attitudes of planar structures and sample locations are indicated. (B) Geological cross-section showing structural features of the Tarlang migmatite-granite complex.

et al., 2015). These findings imply a progressive burial history of Habahe Group rocks to deep crustal levels (30 km or more), during the earliest $D1_B$ event.

D2 deformation in the study area is characterized by upright cylindric F2 folds with NW-SE–trending axial planes and by significant sub-vertical transposition of older foliations by S2 axial planar foliations in the migmatite-granite complex (Jiang et al., 2015). These authors showed that an equilibrium mineral assemblage of garnet, sillimanite, and cordierite is associated with the sub-vertical S2 foliation. Metamorphic phase equilibria calculations indicated that the migmatite recorded an exhumation path evolving from the garnet-sillimanite-K-feldspar stability field (~800 °C/7 kbar) to the garnet-cordierite stability field (680−710 °C/5.5−6.0 kbar) during the D2 event. Previous field mapping also shows that the migmatite-granite complex was emplaced in the core of a regional-scale F2 antiform where un-molten Habahe Group rocks and the Devonian succession occur in the marginal synforms surrounding the limbs of the antiform (Fig. 3, Jiang et al., 2015; Zhang et al., 2015; Wang et al., 2018). The distance from the core to the limb of the antiform is locally less than 1 km, which can be explained either due to thinning of the crust related to $D1_M$ extension, or due to thinning of the limbs caused by D2

post-buckle flattening, or both, as discussed in Jiang et al. (2019).

The D3 fabrics are probably Permian and related to the regional sinistral movements along the Erqis Fault zone to the south (Jiang et al., 2015; Zhang et al., 2015). In the study area, the D3 structure is characterized by the development of a main sinistral shear zone in the northeast (Fig. 3A), as well as a greenschist-facies mylonitic foliation along the contacts between the migmatite-granite complex and the Devonian sequences (Fig. 3A).

The crystallization ages of granites forming the Tarlang migmatite-granite complex range from 425 to 389 Ma, documenting a prominent magmatic activity peaking at the Middle Devonian (Yuan et al., 2007; Zeng et al., 2007; Sun et al., 2008, 2009; Cai et al., 2011b). The anatectic event was coeval with this prominent magmatism and marked by widespread migmatization dated at ca. 390 Ma (zircon U-Pb, Jiang et al., 2010).

3. STRUCTURAL DESCRIPTION OF THE MIGMATITE-GRANITE COMPLEX

In this study, detailed field work was carried out along a section across the Tarlang migmatite-granite complex. On the basis of petrological features, the complex could be subdivided into metatexite, diatexite, and granite zones. In the following subsections, we describe each lithological zone separately.

3.1. Metatexite Zone

The metatexite zone occurs mostly in the southwestern flank of the complex (Fig. 3). These metatexite have two types of protolith. The dominant one is the Habahe Group metasedimentary rocks (including layered metapelite to metagraywacke) and the subordinate phase consists of meta-granites. The metasedimentary rocks are now banded migmatized paragneisses (Sun et al., 2008), and they mainly consist of layered biotite-rich and quartzo-feldspathic bands. The metamorphic index minerals sillimanite and garnet are always present (Fig. 4A). The meta-granites are minor in volume and consist of aligned plagioclase, K-feldspar, biotite, muscovite, quartz, and minor garnet. Irrespective of their protolith, metatexites commonly contain a small proportion of cm-wide leucosomes commonly <20 vol% (Figs. 4A and 4B). Most leucosomes are interlayered with mesosomes, and define an originally sub-horizontal stromatic structure ($S1_M$, Fig. 4B). Rare and narrow biotite-rich, muscovite-bearing, mm- to cm-scale melanosomes occur locally, separating coarse-grained leucosome from mesosome (Fig. 4A). In the leucosome, coarse-grained and euhedral-subhedral K-feldspar and plagioclase crystals constitute the crystal framework while small anhedral quartz are commonly embayed and fill the boundaries between feldspar grains (Fig. 4C), a texture indicative of crystallization from a melt (Sawyer, 2001). In addition, euhedral muscovite and plagioclase crystals define a strong magmatic fabric expressed by a preferred orientation of long axes of these crystals without any plastic deformation and/or recrystallization (Fig. 4D).

In most cases, the horizontal $S1_M$ was folded by F2 folding events and shows variable morphological features (Figs. 5A–5D), controlled by symmetrical, upright, open to tight folds at different scales, with limbs that either dip to the NE or SW (Figs. 6A and 6D). These F2 folds show sub-horizontal hinges with NW-SE strikes (Figs. 6A and 6D). Notably, S1-parallel leucosomes are continuously connected to axial planar leucosomes of F2 folds (Figs. 5A, 5B, and 5D) where they form steeply dipping leucocratic veins that truncate the upright F2 fold (Figs. 5A and 5D). As F2 folds tightened to isoclinal in high strain zones, migmatitic bands were mostly transposed into sub-vertical axial-planar S2 bands (Fig. 5B). These S2 bands dip to the NE at high angles (Fig. 6B). In fold limbs, melt-filled axial-planar foliation may be associated with slip, and may be locally disrupted (Figs. 5C and 6D). Significantly, leucosomes are progressively interconnected as networks that could act as magma migration channels (Figs. 5D and 6D).

3.2. Diatexite Zone

There is a gradual NE-ward increase in leucosome proportions in the migmatite-granite complex, characterized by the transition from a metatexite-dominated zone in the SW to a diatexite-dominated zone in the NE (Fig. 3). The diatexite zone is characterized by a nearly complete transposition of pre-existing $S1_M$ foliation by steep S2 foliation with the presence of leucosomes (Fig. 3). In general, the diatexite contains more than 40 vol% of leucosome (Figs. 7A–7E) and are compositionally heterogeneous, typically composed of coarse-grained plagioclase, K-feldspar, quartz, and muscovite. They commonly show non- or weakly foliated structures including ghost banding and schlieren, related to the disruption of the protolith (Fig. 7A). They also have numerous schollen or rafts of metatexite, varying from cm- to m-scale, in which internal stromatic foliation is preserved (Figs. 7B–7E). In the cores of F2 antiforms, schollen are always elongated preferentially sub-parallel to the regional foliation S2 (Fig. 7C), whereas in the limbs of F2, schollen are rotated and some show sigmoidal shape indicating shearing (Figs. 7D–7F). In addition, these schollen are dismembered to differing degrees, with melt filling the gaps (Figs. 7C–7E). Some diatexite also contains cm-scale, oriented, thin, and elongated schlieren, composed of biotite aggregates associated with garnet, plagioclase, and quartz. They either wrap around schollen or occur as aligned layers helping define a foliation (Figs. 7A, 7C, and 7D). The schlieren can be parallel to sub-vertical S2 foliation in the core of the F2 folds or shallow-dipping in fold limbs (Figs. 7A, 7C, 7D, and 7F). These features collectively indicate that both schollen and schlieren are deformed during pervasive flow of melt. In the core of the complex, the diatexites show magmatic texture characterized by euhedral-subhedral coarse-grained quartz and feldspar crystals and ~120° dihedral angles among them (Fig. 7G). Less commonly in the rim of the complex, sporadically distributed diatexites show much smaller grain sizes associated with lobated grain boundaries indicating grain boundary migration recrystallization mechanism (Fig. 7H). Such differences in the deformation record are probably due to different cooling rates between the core and rim of the complex.

3.3. Granites

The NE-ward transition from the diatexite zone to the granite zone is characterized by gradually decreasing proportions of schollen and schlieren (Fig. 8). These massive granitic bodies either exhibit upward flow as funnel-shaped channels or show vertical drag structures along the contacts with diatexite (Figs. 8A and 8B). These upward flowing granitic magmas commonly truncate $S1_M$ in the neighboring host rock (Fig. 8C). Solidification of granitic magma forms massive, typically coarse-grained granites composed of plagioclase, K-feldspar, quartz, biotite, and muscovite as well as minor garnet (Figs. 8D). Most granites develop a NW-SE–trending sub-vertical magmatic S2 defined by preferred orientation of biotite and feldspar as well as biotite-rich schlieren (Fig. 8E). Alternatively, a subsolidus solid-state S2 foliation commonly developed in the granite bodies that are emplaced along the flanks of the complex (Fig. 8F). In particular, granitic rocks in the core of the complex are characterized by a strong vertical linear fabric (L2) associated with a weak planar fabric (Figs. 9A and 9B). In these rocks, euhedral muscovite, plagioclase, and K-feldspars show preferred alignment (Fig. 9C) but do not define a planar structure, as observed on lineation-normal sections (Fig. 9D). These features are very similar to the deformation patterns of a number of migmatite-granite

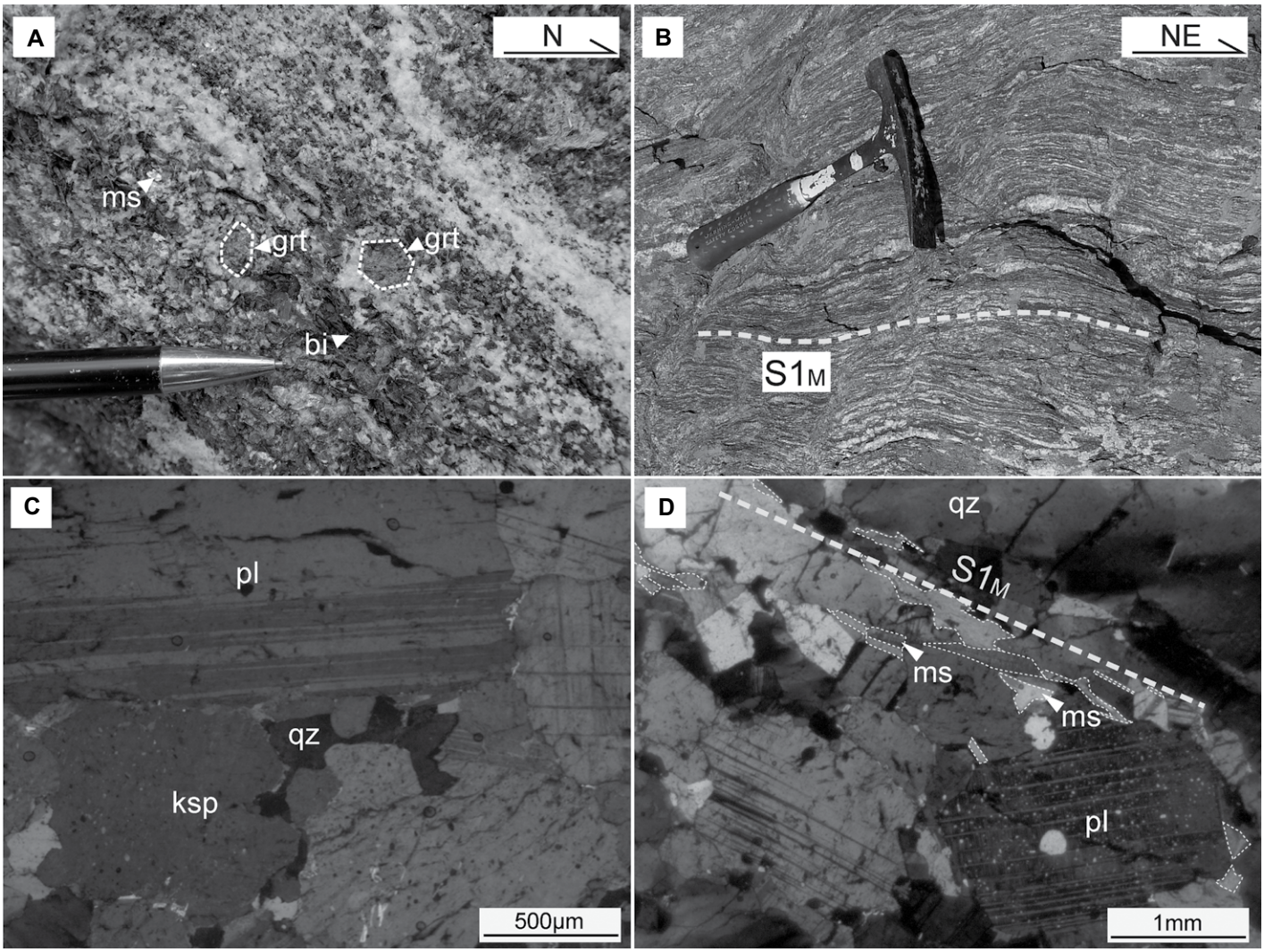

Figure 4. Representative structures of metatexite in the Tralang migmatite-granite complex, western Chinese Altai. (A) Garnet-bearing leucosome layers alternating with mica-rich melanosome layers. (B) $S1_M$ foliation in stromatic metatexite defined by thin leucosome bands alternating with mesosome. (C) Coarse and euhedral to subhedral feldspar with interstitial quartz grains, indicating magmatic crystallization. (D) $S1_M$ foliation defined by the alignment of euhedral crystals of muscovite. The muscovite is outlined by the dash line. Mineral abbreviations: qz—quartz; pl—plagioclase; ksp—K-feldspar; bi—biotite; ms—muscovite.

complexes worldwide (Paterson et al., 1989; Schofield and D'Lemos, 1998; Steenken et al., 2000; Žák et al., 2012), where they have been interpreted as indicative of syntectonic emplacement of magmas (Paterson et al., 1989; Schofield and D'Lemos, 1998). Besides, granites that intruded the Habahe Group metamorphic envelope, particularly the Qiongkuer pluton in the northeast, commonly develop a significant solid-state foliation that is continuous with the regional S2 foliation (Fig. 3).

Apart from these granites, some dm- to m-wide muscovite-bearing granitic dykes intrude the surrounding metamorphic envelope with sharp, planar borders (Figs. 9E and 9F). These dykes display weak magmatic foliation and are emplaced parallel to the regional S2 foliation, as it is typical of structure-controlled intrusions emplaced into cool surrounding rocks.

4. U-Pb ZIRCON GEOCHRONOLOGY

In order to provide further geochronological constraints on the evolution of the complex, representative samples selected from the mesosome of the metatexite (15BU04, 15BU05), the diatexite migmatite (12BU14, 12BU102), and the anatectic S-type granite (11BU26, 16BU30), as well as the late granitic dyke (12BU103, 12BU18) were dated using zircon U-Pb method (Figs. 10–12). Locations of the samples were indicated in Figure 3.

4.1. Analytical Methods

Zircon grains were extracted using standard heavy liquid and magnetic techniques and then randomly hand-picked under a binocular microscope. These grains were then mounted in epoxy resin and polished. The internal structures of the grains were checked by cathodoluminescence imaging, using a JXA-8100 electron probe microanalyzer equipped with a Mono CL3 cathodoluminescence system installed at the Guangzhou Institute of Geochemistry, Chinese Academy of Sciences (GIG-CAS).

Samples 16BU30, 11BU26, 12BU14, 12BU102, 12BU103, and 12BU18 were dated using a pulsed Resonetic 193 nm ArF excimer

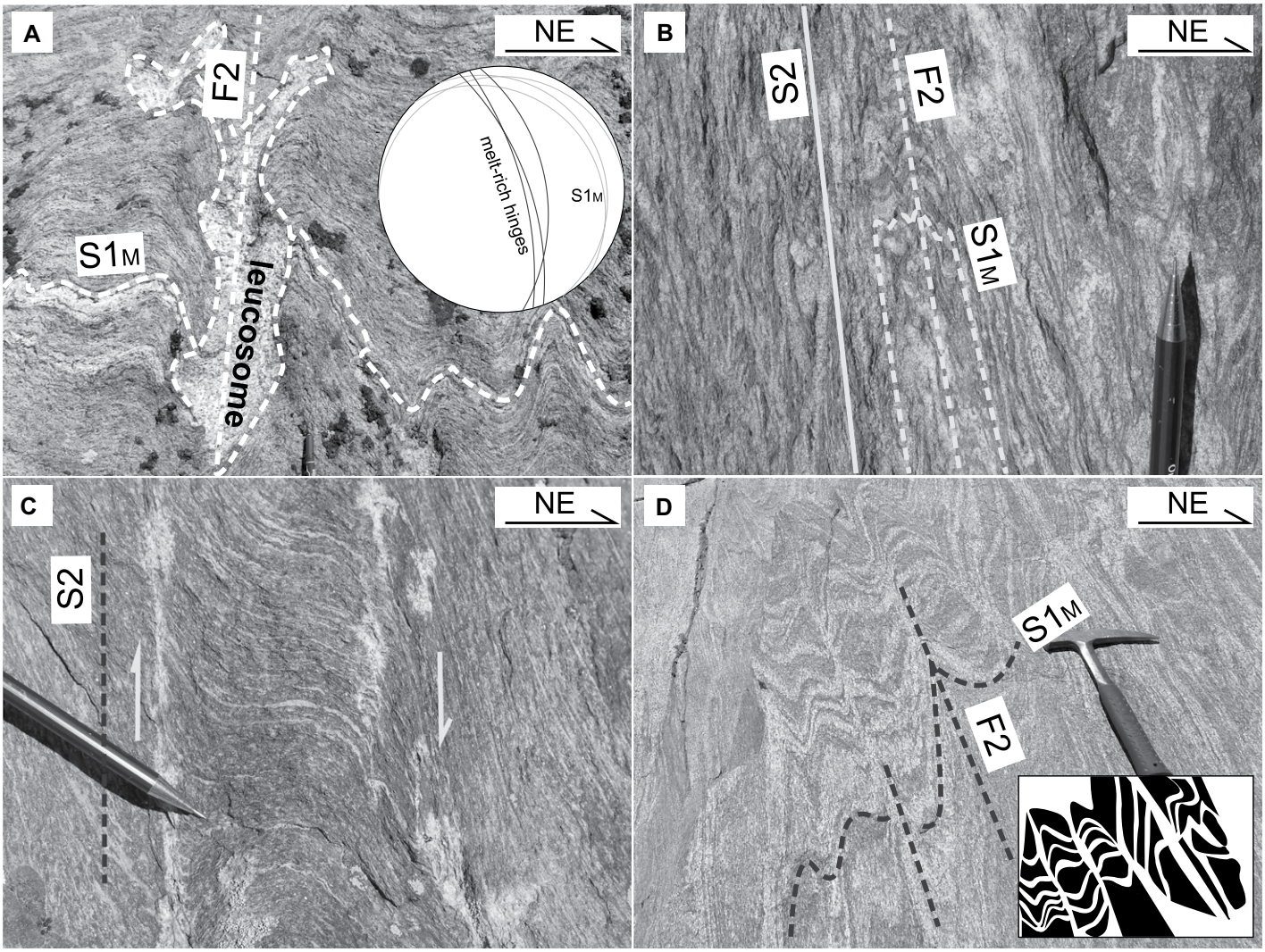

Figure 5. Representative structures of metatexite in the Tralang migmatite-granite complex, western Chinese Altai. (A) Folded stromatic metatexites layers are locally truncated by leucosome veins that are parallel to F2 axial planes. The insert stereonet shows relations between S1 stromatic bands and F2 axial planar bands. (B) Folded stromatic migmatite showing transposition of S1 foliation in D2 high-strain zones. (C) Melt-filled leucosome bands slipped in the limb of F2 fold. (D) Folded stromatic migmatite associated with the development of F2 axial plane leucocratic veins that form interconnected networks.

laser ablation system coupled with an Agilent 7500a inductively coupled plasma–mass spectrometer at GIG-CAS. All analyses were carried out with a diameter of 29 μm, 10 Hz repetition rate, energy of 80 mJ per pulse, and ablation time of 40 seconds. Purified helium was used as the carrier gas. Zircon standard 91500 (Wiedenbeck et al., 1995) was used for calibration, and the standard silicate glass NIST610 was used to calculate the Th and U concentration. The detailed analytical procedure was described by Li et al. (2012). The raw data were calculated by ICPMSDataCal 9.0 (Liu et al., 2008) and age calculations and concordia plots were processed using Isoplot 4.15 (Version 4, Ludwig, 2003).

Zircon U-Pb dating of samples 15BU04 and 15BU05 used a Cameca IMS-1280 secondary ion mass spectrometer ion microprobe established at GIG-CAS following the analytical method described by Li et al. (2009). Zircon standards Plešovice (Sláma et al., 2008) and 91500 (Wiedenbeck et al., 1995) were used for calibration. Measured compositions were corrected for common Pb using non-radiogenic ^{204}Pb, assuming that for low counts of ^{204}Pb, common Pb is mainly surface related (Ireland and Williams, 2003) and has a composition of present-day average crustal composition (Stacey and Kramers, 1975). The data reduction was carried out using the in-house geochronology software of Dr. Martin Whitehouse (Whitehouse et al., 1999). Off-line data were calculated and plotted using Isoplot 4.15 (Version 4, Ludwig, 2003). Note that for better weighted mean age calculating, the age results less than 90% concordant were excluded for plotting. The dating results are listed in Supplemental Table S1.[1] All ages are quoted with 1σ uncertainty.

4.2. Results

Nearly all samples contain abundant magmatic zircons characterized by concentric oscillatory zoning (Figs. 10, 11, and 12). Apart from these typical magmatic zircons, a subordinate

[1]Supplemental Material. GPS coordinate and zircon U-Pb data of samples. Please visit https://doi.org/10.1130/GSAB.S.13724509 to access the supplemental material, and contact editing@geosociety.org with any questions.

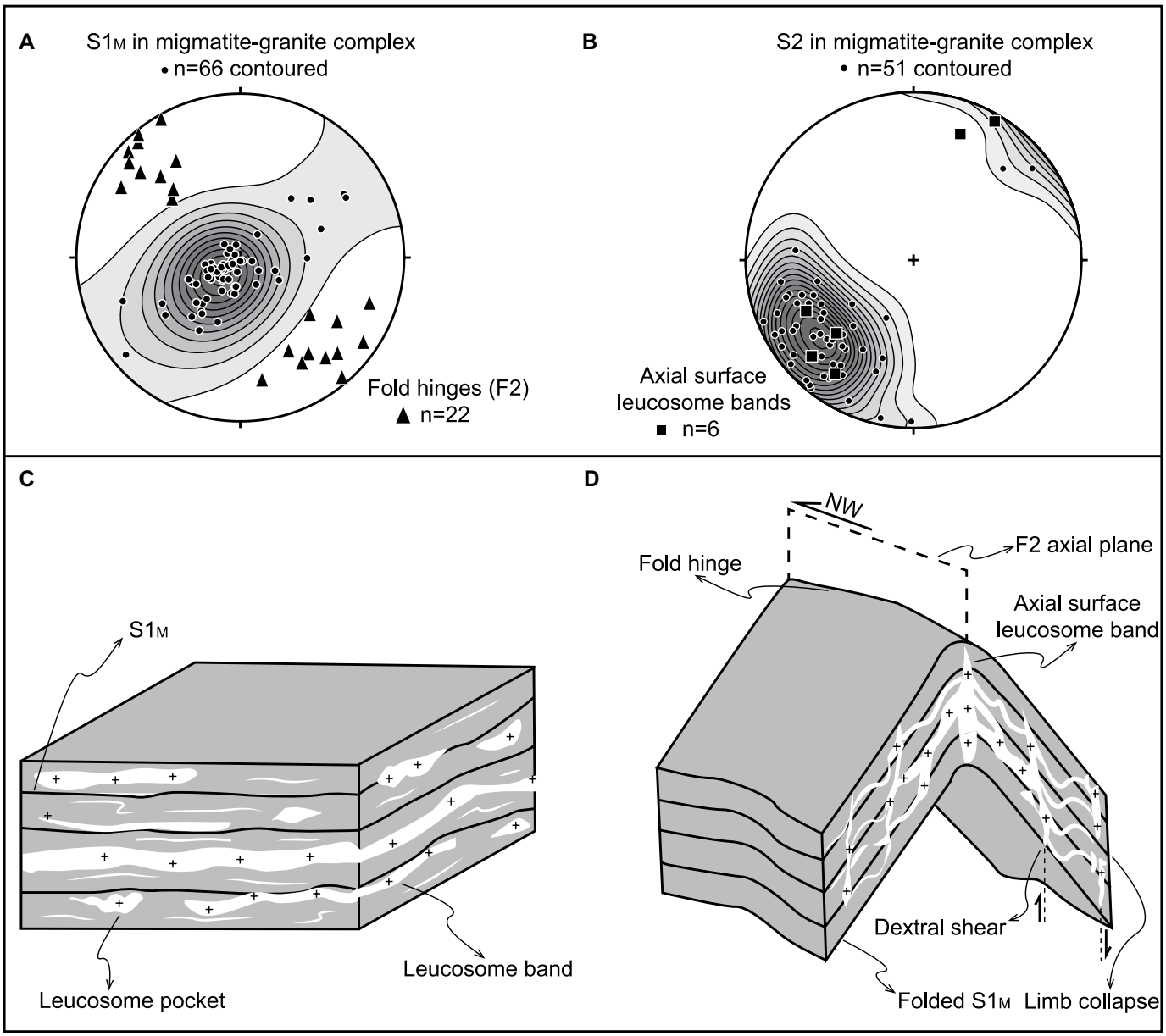

Figure 6. Stereographic projections of foliations from the Tarlang migmatite-granite complex, western Chinese Altai. (A) Stereonets of poles of S1 foliations (contoured) and attitudes of F2 hinges. (B) Stereonets of poles of S2 foliations (contoured) and F2 axial surface leucosome bands. All stereonets are lower-hemisphere projections. (C–D) Schematic diagrams show migmatite evolution associated with $D1_M$ and D2 phases of deformation: (C) Development of sub-horizontal leucosome bands and roughly aligned elongated leucosome pockets during D1; (D) Leucosome bands were folded and magma migrated toward the hinge zones forming axial surface leucosome bands during D2. A few axial surface leucosome bands on fold limbs acted as shear planes during F2 folding (modified after Symington et al., 2014; Martini et al., 2019a).

group of zircons with much more complicated internal structures are also present. They commonly have inherited cores, that is, corroded, fragmented, or rounded cores surrounded by weakly zoned rims (Figs. 10B and 11B). Less commonly, some grains are apparently high or very low luminescent thus, hardly revealing any internal structures. Given that the current study focuses on the formation and migration of the magmas forming the Tarlang migmatite-granite complex, only typical magmatic zircons were dated and are introduced in the following section. However, U-Pb ages of the remaining zircon populations were already investigated by previous geochronological studies in the region which revealed their dominantly Cambrian–Ordovician ages (e.g., Cai et al., 2011b). Such an age range is in accordance with the most common ages of the detrital zircons in the Ordovician Habahe Group metasedimentary rocks (e.g., Sun et al., 2008; Jiang et al., 2011) and hence were interpreted as inherited zircons (Sun et al., 2008; Cai et al., 2011b).

4.2.1. Mesosome of Stromatic Metatexite (Samples 15BU04 and 15BU05)

Samples 15BU04 and 15BU05 are granitic mesosomes that show sub-horizontal migmatitic foliations. Zircons from these samples range from 100 to 400 μm in length and have length/

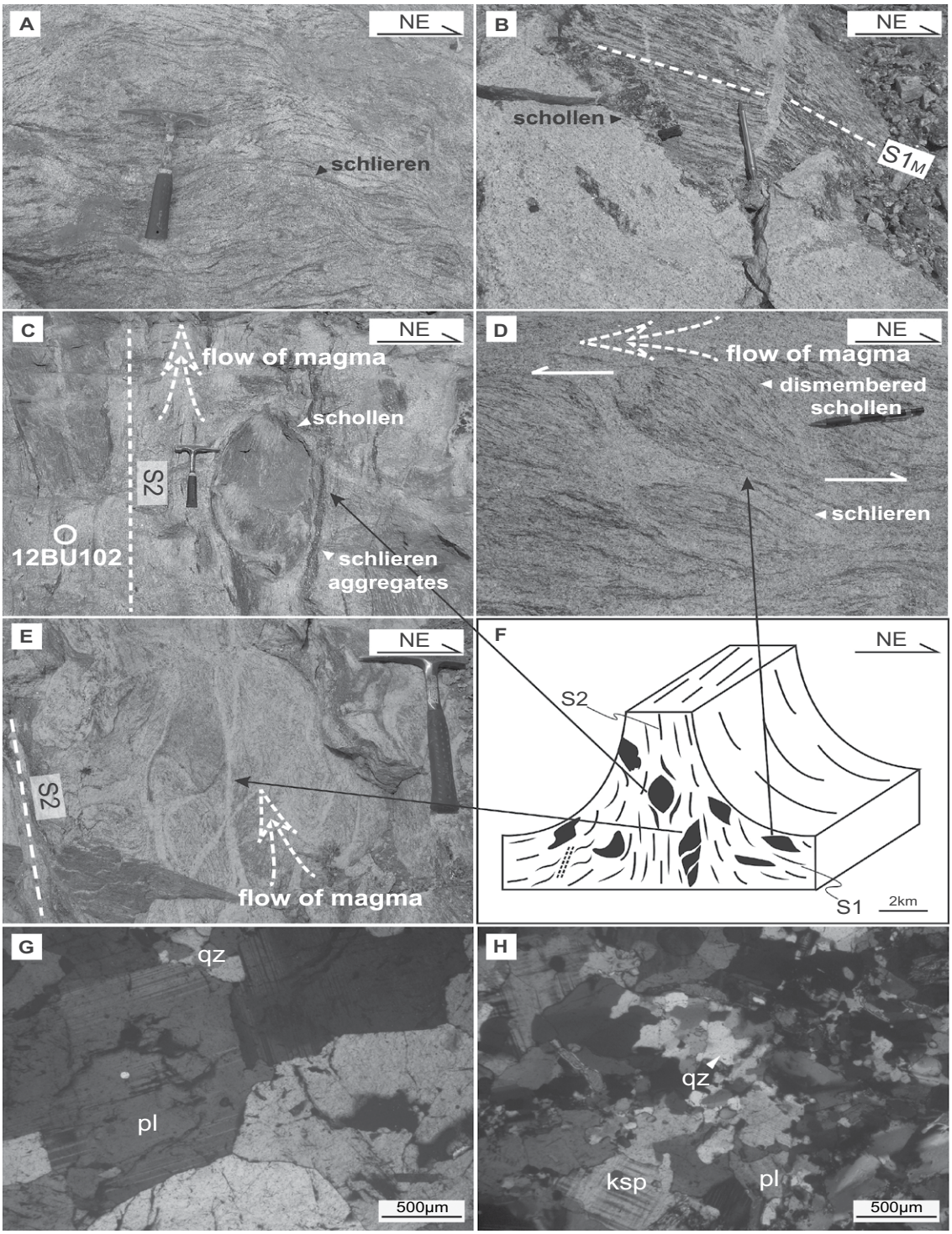

Figure 7. Representative structures of diatexite in the Tralang migmatite-granite complex, western Chinese Altai. (A) Perturbed schlieren diatexite containing aligned schlieren that are oblique to the S2 foliation. (B) Schollen in diatexite with internal structures similar to those in metatexites. (C) Schollen diatexite in the core of a F2 antiform. Note that these schollen are elongated and parallel to sub-vertical S2 and wrapped by sub-vertical schlieren. (D) Flow banding indicated by orientations of elongated and dismembered schollen in diatexite. Some schollen are dismembered into small schlieren. Note that schollen here are sigmoidal indicating oblique shear sense with respect to S2. (E) Flow of magma in diatexite near the F2 fold hinge. Note that the schollen here have sigmoidal shapes indicating S2-parallel sub-vertical shearing. (F) A schematic diagram showing variable features of schollen and schlieren in different structural positions with respect to vertical flow of diatexite. (G) Photomicrograph of schollen diatexite showing that coarse-grained feldspar crystals have straight boundaries and quartz crystals show rational faces suggesting magmatic crystallization, and (H) photomicrograph of diatexite showing medium-grained quartz and feldspar crystals recording grain boundary migration indicated by lobate boundaries between quartz grains, a typical feature of solid-state recrystallization. Mineral abbreviations are the same as in Figure 6.

width ratios varying from 1:1 to 4:1. All zircons in sample 15BU04 have magmatic concentric oscillatory zoning with thin metamorphic rims (Fig. 10A) while those in sample 15BU05 also show magmatic zoning but a few have inherited cores (Fig. 10B). Fifteen spots on the oscillatory zoned portion of different grains for each sample were analyzed. Zircon U-Pb analysis of these two samples yielded single and tight populations, with weighted mean $^{206}Pb/^{238}U$ ages of 416 ± 5 Ma and 411 ± 5 Ma (Figs. 10A and 10B). Two spots in sample 15BU04 and one spot in sample 15BU05 were excluded from age calculation because of low concordance (less than 90% concordant, Table S1 [see footnote 1]).

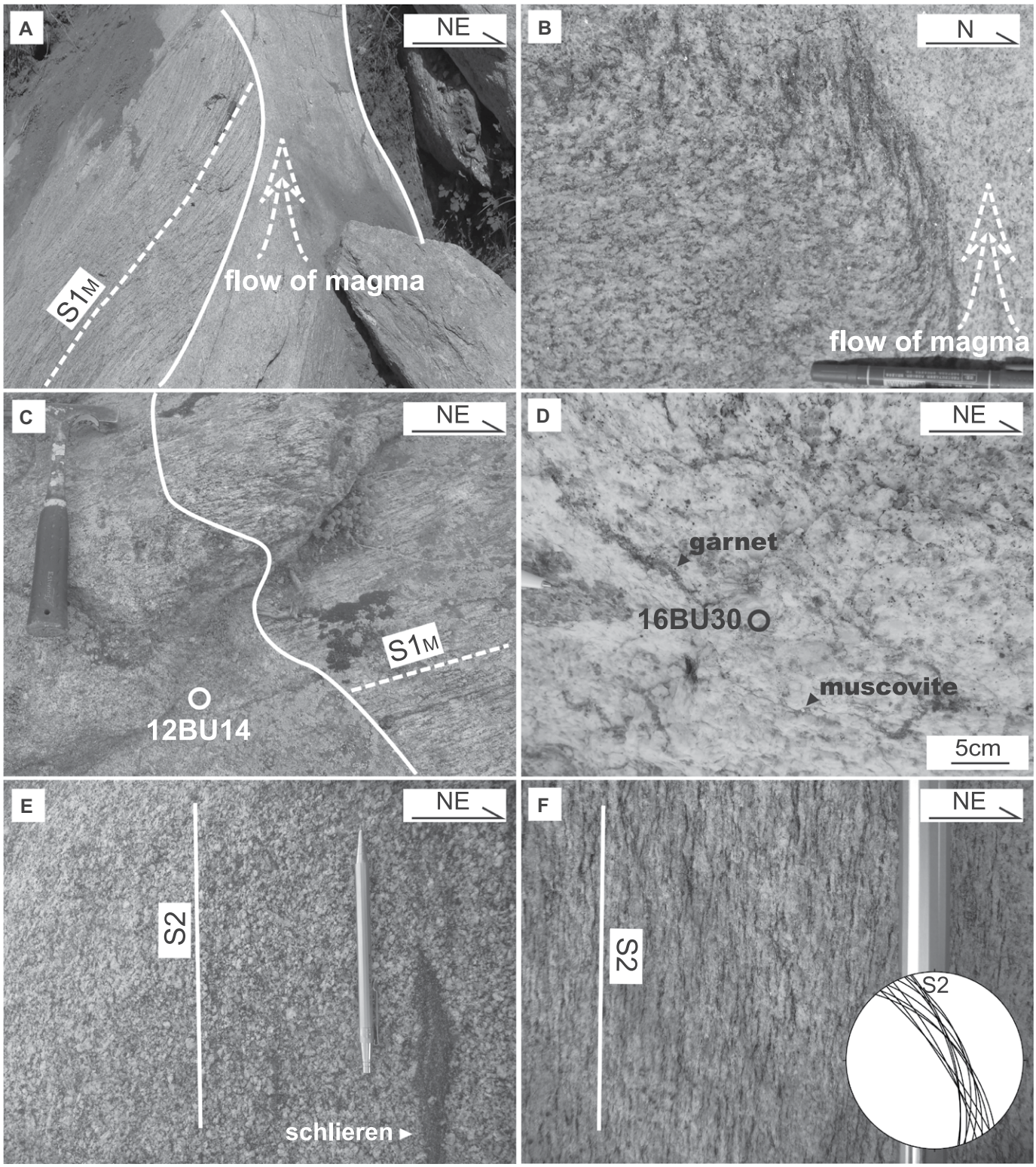

Figure 8. Representative structures of diatexite/granite in the Tralang migmatite-granite complex, western Chinese Altai. (A) Funnel-shaped diatexite showing dragging of foliation indicative of upward flow of magma. (B) Drag structure in the contact between two different phases of granite indicating upward movement of magma. (C) Massive diatexite crosscuts a stromatic orthogneiss. Note location of sample 12BU14 for U-Pb zircon dating is also indicated. (D) Garnet- and muscovite-bearing leucogranite. Sample 16BU30 collected for dating is also indicated. (E) Schlieren granite with schlieren elongated parallel to magmatic fabric (S2). (F) Sub-vertical solid-state S2 foliation defined by preferred orientation of elongated quartz, feldspar, and mica in a two-mica granite. Insert: stereonet showing attitudes of solid-state S2 foliations.

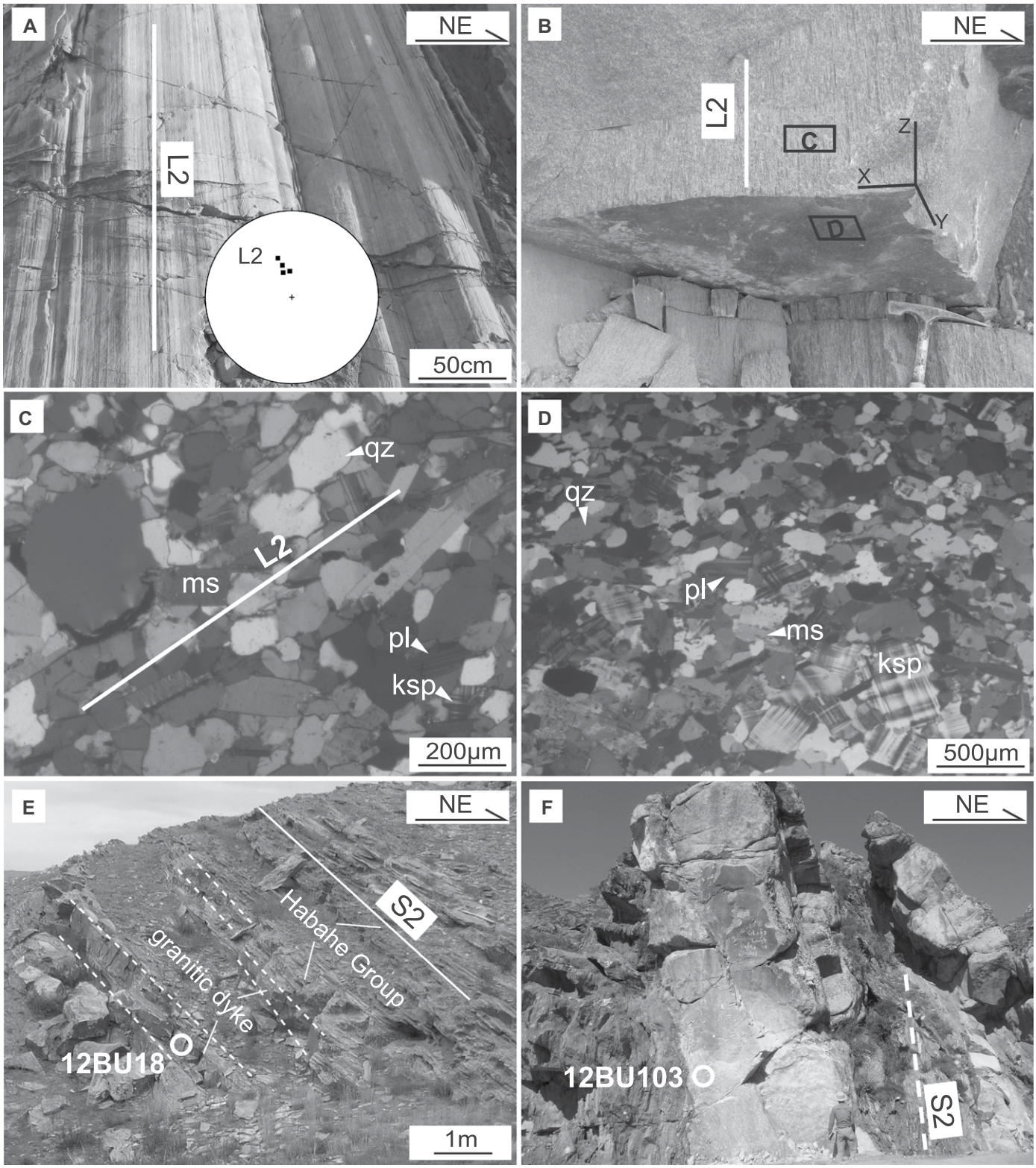

Figure 9. (A) Linear fabric in the granites in the core of the Tarlang migmatite-granite complex, western Chinese Altai. An insert stereonet shows attitudes of the linear fabrics. (B) Sub-vertical lineation L2 forms a strong linear fabric in granite in the core of the Tarlang migmatite-granite complex. Locations for (C) and (D) are indicated. (C) Photomicrograph of the X-Z section shows L2 lineation defined by the alignment of euhedral crystals of muscovite (ms), plagioclase (pl), K-feldspar (ksp), and quartz (qz). (D) Photomicrograph of the X-Y section lacking preferred orientation of qz, pl, ksp, and ms. (E–F) Macroscale late-stage muscovite-bearing granitic dykes (white) intruded into the Habahe Group (gray) with sharp boundaries. Samples 12BU18 and 12BU103 collected for U-Pb zircon dating are indicated.

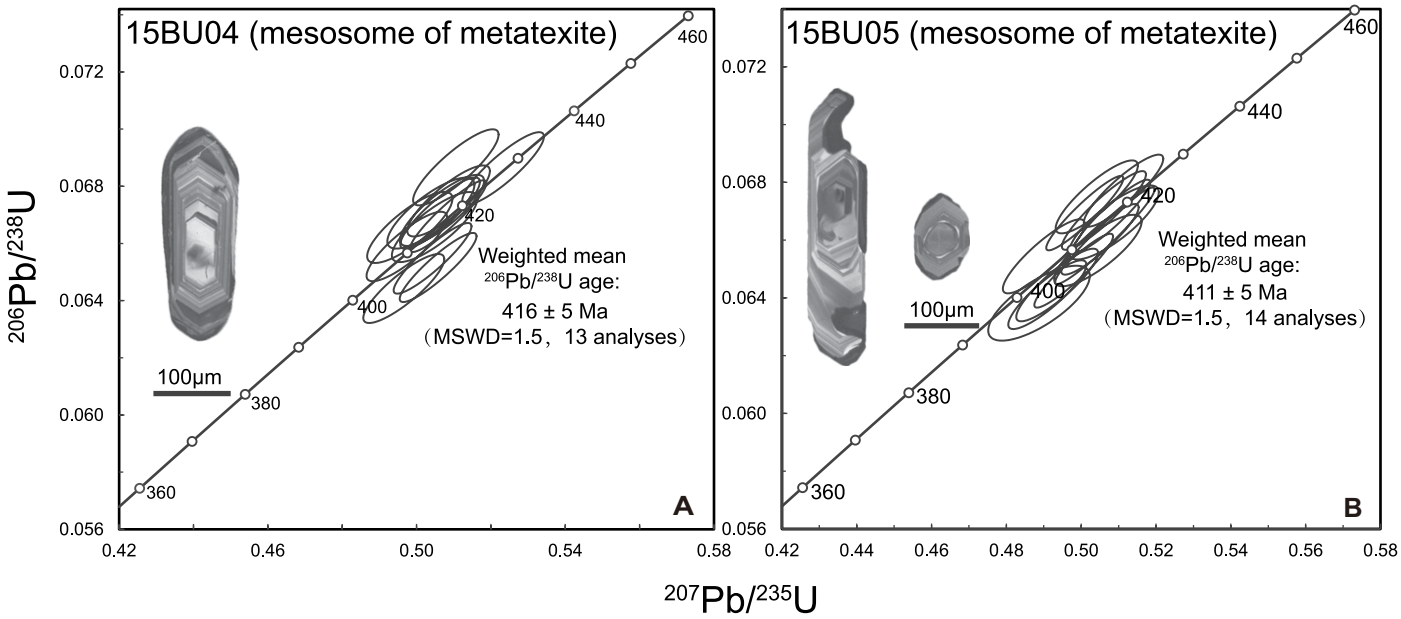

Figure 10. (A–B) U-Pb concordia diagrams for zircons from mesosome samples 15BU04 and 15BU05 of metatexites (see Fig. 3 for sample location). MSWD—mean square weighted deviation.

4.2.2. Diatexite Samples 12BU14 and 12BU102

Sample 12BU14 is a massive diatexite that has a steep flow foliation crosscutting stromatic $S1_M$ fabric in the neighboring metatexite (Fig. 8C). Zircons from this sample are predominantly euhedral to subhedral, ranging from 100 to 500 μm with length/width ratios between 2:1 and 4:1. Most zircon grains have concentric oscillatory zoning with thin dark metamorphic rims and less commonly inherited cores preserved (Fig. 11A). Laser ablation–inductively coupled plasma–mass spectrometry analyses of zoned domains of 30 zircon grains yielded a single and tight age population with a weighted mean $^{206}Pb/^{238}U$ age of 403 ± 1 Ma (Fig. 11A) after four discordant spots were excluded.

Sample 12BU102 is a diatexite with schollen and schlieren. Its schollen have vertical elongated shape and its schlieren are also vertically aligned, roughly parallel with the S2 foliation of the host migmatite (Fig. 7C). Zircons from this sample show euhedral to subhedral shapes, ranging from 100 to 300 μm with length/width ratios between 1:1 and 4:1. Most of them have concentric oscillatory zoning with thin and dark metamorphic rims and some have inherited cores (Fig. 11B). Zircon U-Pb isotopic analyses of zoned domains of 30 grains were carried out. Data of 26 analyses formed three clusters with weighted mean $^{206}Pb/^{238}U$ ages of 391 ± 2 Ma, 412 ± 1 Ma, and 422 ± 2 Ma (Fig. 11B). Another four analyses were not considered in the age calculation due to low concordance.

4.2.3. Leucogranite Samples 11BU26 and 16BU30

Leucogranite samples 11BU26 and 16BU30 were collected from a garnet-bearing phase of the dominant diatexite-granite body. These leucogranites show a diffuse boundary against the host diatexite. They consist mainly of plagioclase, quartz, muscovite, <5 vol% biotite and accessory garnet (Fig. 8D), and are considered to have originated from the anatexis. Zircon crystals from these samples vary from euhedral to anhedral in shape and 100–500 μm in length, and have length/width ratios ranging from 1:1 to 4:1. They commonly have inherited cores and show variable internal structures, including oscillatory zoning in some grains and metamict structures in others (Figs. 11C and 11D). Twenty-five spots were analyzed in zoned zircon domains of sample 11BU26. Except for four less-concordant spots, the remaining 21 analyses yielded concordant ages with a weighted mean $^{206}Pb/^{238}U$ age of 413 ± 1 Ma (Fig. 11C). Twenty concordant analyses in zoned zircon domains from sample 16BU30 defined a single age population with a weighted mean $^{206}Pb/^{238}U$ age of 402 ± 3 Ma (Fig. 11D).

4.2.4. Late Muscovite-Bearing Granitic Dykes Samples 12BU18 and 12BU103

The late muscovite-bearing granitic dykes (sample 12BU18 is from the adjacent Qiongquer area, and displays the same feature as sample 12BU103 from the Tarlang complex; see Figs. 3B, 9E, and 9F), consist mainly of muscovite, garnet, plagioclase, and quartz and were emplaced as m-scale dykes (Fig. 9F). Zircons from these samples are predominantly euhedral to subhedral, range from 100 to 300 μm with length/width ratios varying from 1:1–4:1. Some of them have uniformly oscillatory zoning while others have inherited cores. Nearly all of them have thin dark rims (Figs. 12A and 12B). Twenty-five analyses were performed on the oscillatory zoning portions of zircons for each sample. Except for a few strongly discordant analyses (concordance < 90%), 23 analyses of sample 12BU18 form two age populations, with weighted mean $^{206}Pb/^{238}U$ ages of 391 ± 1 Ma and 372 ± 4 Ma (Fig. 12A). Twenty analyses of sample 12BU103 also form two clusters with weighted mean $^{206}Pb/^{238}U$ ages of 396 ± 2 Ma and 420 ± 1 Ma (Fig. 12B). Moreover, a few grains from this sample gave concordant to slightly discordant ages of ca. 360 Ma (Fig. 12B), similar to the youngest age population of sample 12BU18.

5. DISCUSSION

5.1. Migration of Magmas and Emplacement of Granites

The Tarlang migmatite-granite complex represents a major exhumed high-grade core within the Altai accretionary wedge. The emplacement of the complex has previously been discussed in the context of regional deformation reconstructions (Jiang et al., 2015, Zhang et al., 2015), however, the detailed processes that drove migration of anatectic magmas to shallow,

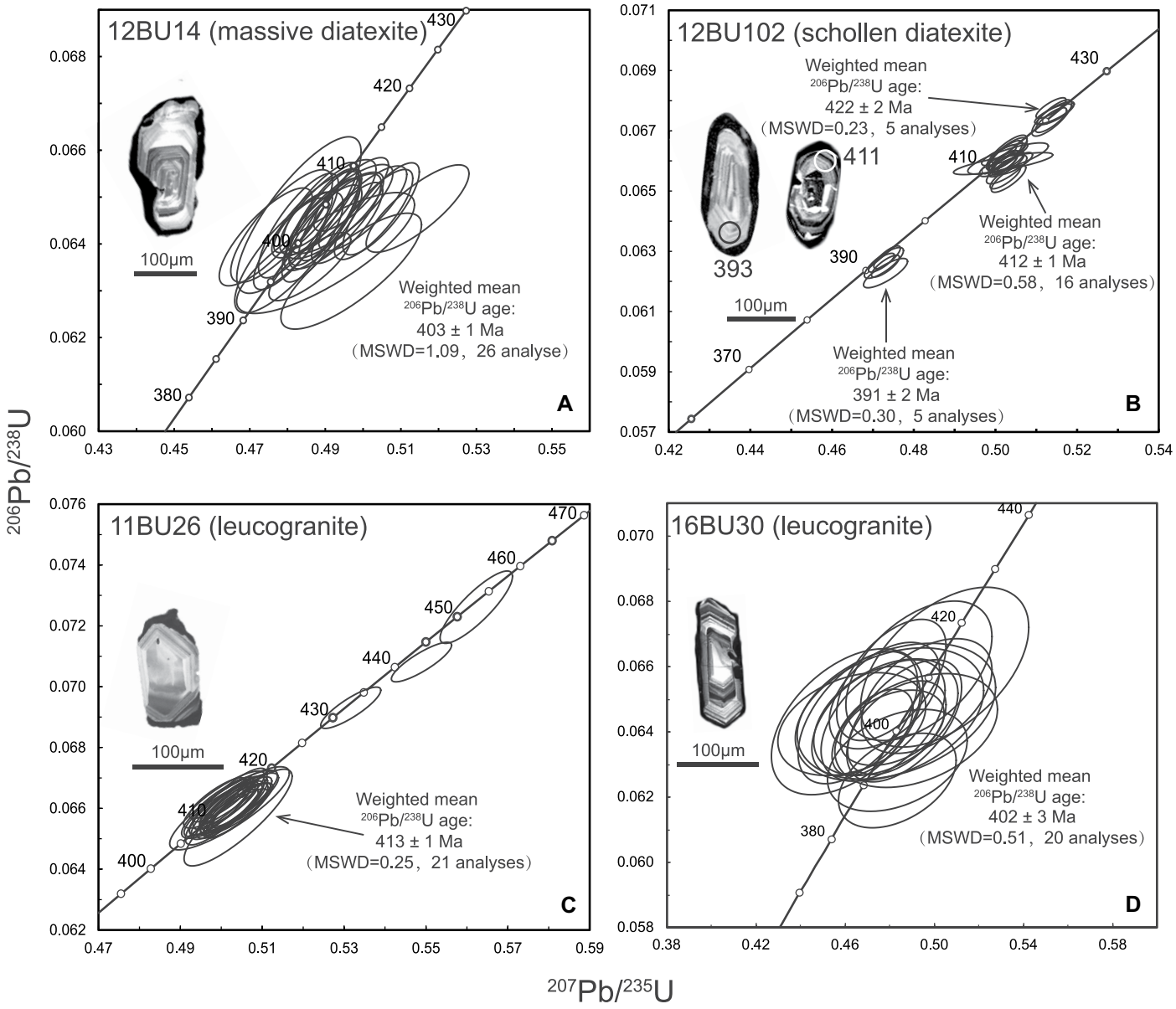

Figure 11. U-Pb concordia diagrams for zircons from: (A) massive diatexite sample 12BU14 (see location in Fig. 3 and texture in Fig. 8C). (B) Schollen diatexite sample 12BU102 (see location in Fig. 3 and texture in Fig. 7C). (C–D) leucogranite samples 11BU26 and 16BU30 (see location in Fig. 3 and texture in Fig. 8D). MSWD—mean square weighted deviation.

un-molten crustal levels and formed the complex remain poorly understood. This issue can be addressed using the structural and petrological observations presented in this study.

We first focus on the oldest sub-horizontal fabric $S1_M$ in the metatexites, where melts segregated into leucosome (Fig. 4B) suggesting that their segregation was principally controlled by sub-horizontal extension and foliation anisotropy. These pervasive leucosome bands (Figs. 4B and 5A−5D) exhibit well-developed magmatic fabric (Figs. 4C and 4D). Following the interpretation in Jiang et al. (2019), we conclude that the S1-parallel leucosome bands and lenses highlight the effects of extensional deformation on melt extraction, with vertical shortening helping to squeeze melt out of the compacting matrix (melanosome), similar to those described in Sawyer (1994), Sawyer (1996), and Weinberg et al. (2015).

As it is shown in the metatexite, the anatectic Habahe Group rocks associated with horizontal migmatite bands ($S1_M$) commonly have <20 vol% leucosome (e.g., Fig. 4B). More melt is required to breakdown the solid framework of the migmatites and allow them to flow en masse as a magma, as observed in the diatexite zone (Figs. 7A–7E). Therefore, an additional mechanism should be considered to enhance melt availability. It has been demonstrated that structure-controlled redistribution of melt within a melting system could locally create high melt content domains (Sawyer, 1996, 1998), and eventually trigger diapiric rise (e.g., Brun, 1980; Coward, 1981; Faure et al., 1986; Clos et al., 2019).

Folding has been considered as a major structural mechanism responsible for mobilization of deep molten crust (Gates, 1987; Allen et al., 2001; Fowler and Osman, 2001). It has been documented that folding creates pressure gradients that force melt migration toward antiform hinge zones (Weinberg and Mark, 2008;

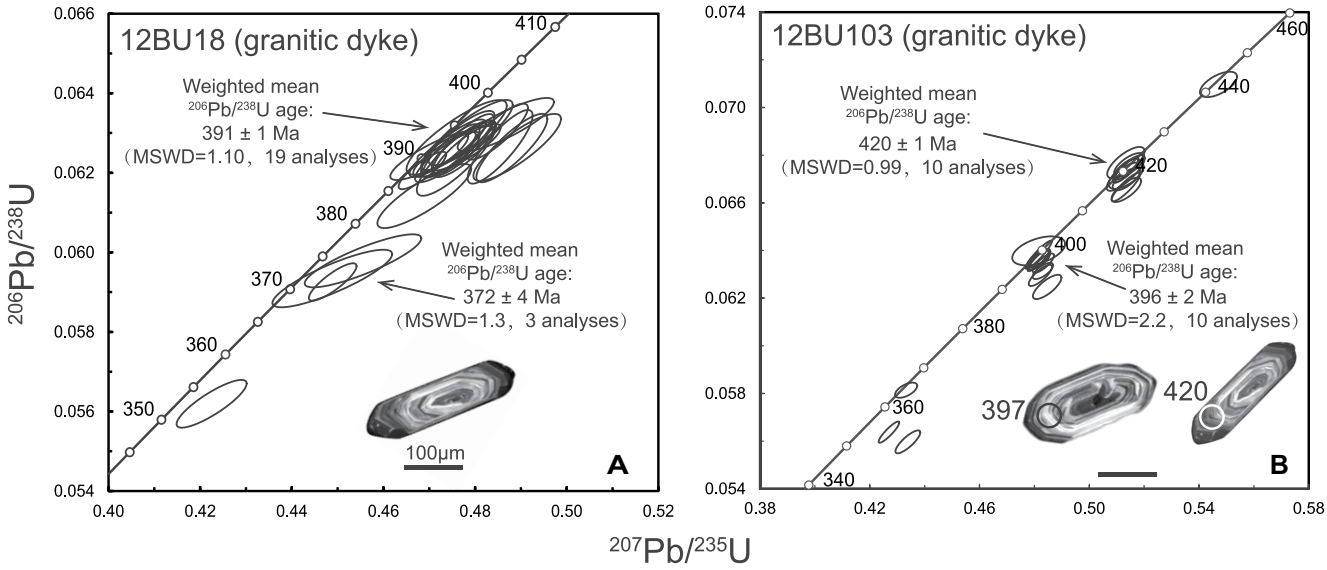

Figure 12. (A–B) U-Pb concordia diagrams for zircon from late-phase granitic dykes 12BU18 and 12BU103 (see location in Fig. 3 and texture in Figs. 9E and 9F). MSWD—mean square weighted deviation.

Weinberg et al., 2013). In addition, folding could create a network of pathways allowing magma ascent (Sawyer, 1998; Weinberg and Mark, 2008; Weinberg et al., 2013; Martini et al., 2019b). In this study, such a network is characterized by sub-horizontal foliation-parallel leucosomes linked with vertical axial planar leucosomes formed during F2 folding (Figs. 5A−5D and 7B). Once the network formed, magma extraction became effective, draining melt rapidly from the S1 foliation and driving it toward the F2 hinge zones. This process might also have progressively transposed the sub-horizontal stromatic $S1_M$ fabric into the new sub-vertical S2 (Fig. 5B). Notably, upward magma movement in antiformal hinge zones of F2 folds is indicated by sigmoidal-shaped schollen (Figs. 7C–7F), funnel-shaped channels of diatexite associated with drag folding at their contacts (Figs. 8A and 8B), as well as significant sub-vertical magmatic foliations and strongly lineated granitic rocks (Figs. 8E, 9A, and 9B). We, therefore, conclude that the D2 contraction caused upright folding and gave rise to the leucosome network and pressure gradients that lead magma to flow toward the lower-pressure zones in the hinges of antiforms and upwards through the crust. This flow ultimately led to the emplacement of the migmatite-granite complex in the core of a large-scale antiform. Magma diapirism has been considered essential for magma upward migration (Whitney et al., 2004). However, such a mechanism may not be the major cause for the formation of the Tarlang migmatite-granite complex. This is because a typical diapiric molten crust, driven by buoyancy alone, would exhibit circumcentric or radial structures (such as lineations), as well as diapir-up kinematics in relation to the country rocks (Dixon, 1975; Cruden, 1988; Kratinová et al., 2006), whereas the Tarlang complex is characterized by NW-SE–trending cylindrical upright folds (Fig. 7, see also Jiang et al., 2015; Zhang et al., 2015). We argue that formation of the complex can be best explained by the development of antiformal folds accompanied by magma migration toward hinge zones amplified by buoyancy forces. This process of folding assisted by buoyancy and diapirism has been inferred as the main mechanism driving the ascent of molten crustal components in many anatectic terranes (e.g., Ramberg, 1980; Faure et al., 1986; Maierová et al., 2014; Clos et al., 2019).

In conclusion, migration of magma in the Tarlang migmatite-granite complex developed over two main stages. The first stage was characterized by deep crust anatexis associated with horizontal extension and segregation of melt into the S1-parallel sub-horizontal leucosome lenses or bands. The second stage was characterized by D2 upright folding giving rise to a network of leucosomes associated with melt migration from layer-parallel leucosomes to axial planar foliation (S2) ones. This process accounted for magma accumulation toward F2 hinge zones, and, eventually, vertical flow of molten crust from deep to shallow crustal levels within or along F2 antiformal hinges.

5.2. Geochronological Constraints on the Evolution of the Tarlang Migmatite-Granite Complex

Previous geochronological studies revealed granites formed from 425 to 389 Ma in the study area (Yuan et al., 2007; Sun et al., 2008; Cai et al., 2011b; Jiang et al., 2015; Zhang et al., 2015). Our data also yielded a succession of ages spreading from 432 to 364 Ma, most of which are between 423 and 384 Ma (Fig. 13). This age range consists of several age populations and many samples contain two or three zircon populations (Figs. 11B and 12) suggesting long-lasting melting events. Similar age patterns are commonly seen in stretched backarcs where massive and cyclic melting events developed (e.g., Cavalcante et al., 2018; Wolfram et al., 2019; Farias et al., 2020). Results presented in the previous sections allow reconstruction of the spatial and temporal evolution of the metatexite-diatexite-granite succession investigated.

It has been suggested that the migmatite-granite rocks investigated were derived from the partial melting of Habahe Group rocks (Sun et al., 2008; Jiang et al., 2015; Zhang et al., 2015). The youngest detrital zircon population found in the Habahe Group metasedimentary rocks is ca. 438 Ma (Long et al., 2010). Following these detrital ages, the oldest magmatic zircon age population in the migmatite-granite complex is 420−410 Ma (Figs. 10, 13, and 14). This age population is common in the granitic mesosome of the metatexite that exhibits a sub-horizontal S1 foliation (samples 15BU04 and 15BU05; Figs. 10A and 10B). It is also present in the studied diatexites and granites, both of which have $S1_M$ relic schollen and schlieren (samples 12BU102 and 11BU26; Figs. 11B and 11C). The 420−410 Ma age population is therefore interpreted as recording the timing of formation of melt-present sub-horizontal S1 foliation,

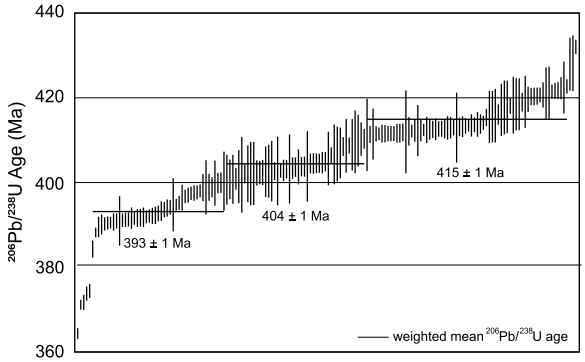

Figure 13. Plots of zircon ages for all analyzed samples. Three discrete age populations can be distinguished indicating a continual but multiphase magmatic evolution history of the Tarlang migmatite-granite complex, western Chinese Altai.

assigned as the first stage in the evolution of the complex ("stage 1" in Fig. 15).

The second major age population is 410−400 Ma (Figs. 11A, 11C, 11D, 13, and 14), which was obtained from diatexite samples, including massive diatexite veins (e.g., sample 12BU14; Figs. 8C and 11A) and granitic leucosomes (e.g., samples 16BU30, 11BU26; Figs. 8D, 11C, and 11D). These diatexites either crosscut early sub-horizontal fabric $S1_M$ or encompass a large amount of schollen (Fig. 14). These features suggest that the diatexites were emplaced when the protolith started to lose coherence associated with the formation of the drainage network ("stage 2" in Fig. 15). Thus, this second age population is considered to reflect the beginning of D2 folding, as zircons crystallized during the maturation of the drainage network.

Folding and magma migration led to the loss of the solid framework of the migmatites. Once this happened, bulk upward flow of the partially molten crust could occur. Ascent and emplacement of anatectic magma in the core of regional F2 antiforms forming massive diatexites and granites characterize "stage 3" in Figure 15. The schollen diatexite sample 12BU102, collected from the core of the F2 antiform (Figs. 7C and 7F), yielded a younger zircon U-Pb age of 391 ± 2 Ma (Figs. 11B and 14). This age is interpreted as a record that the vertical flow of the anatectic orogenic lower crust lasted at least until that time. This is consistent with the interpretation of Zhang et al. (2015) who reported a ca. 389 Ma granite originated from vertical extrusion of magmas in the region. Accordingly, the magma upward migration stage, assisted by D2 deformation, can be constrained to have lasted from 410 to 390 Ma. This is consistent with the idea that F2 upright folding occurred between 400 and 380 Ma in other parts of the Chinese Altai (Jiang et al., 2015, 2019).

The youngest age group, ranging from 372 Ma (sample 12BU18) to ca. 360 Ma (sample 12BU103B), was obtained from the structurally controlled granitic dykes (Figs. 9E, 9F, 12, 13, and 14). These dykes may represent the residual melt after solidification of the core of the complex and emplaced into cooled rocks, probably during the waning stage of migmatization ("stage 4" in Fig. 15). Their ages therefore post-date the emplacement of the migmatite-granite complex and the main stage of D2 deformation.

5.3. Crustal Flow in the Accretionary Orogenic System

Crustal flow developed pervasively in orogens associated with large-scale movement of melt-weakened crust (Beaumont et al., 2001; Whitney et al., 2004; Farias et al., 2020; Kang et al., 2020). Partial melting changes the rheology and density of the crust and leads to mechanical decoupling between molten layers and bounding lithologies because decreased viscosity enables crustal flow under weak driving forces (Holtzman et al., 2005; Rosenberg and Handy, 2005). Recent geological observations (Schulmann et al., 2008; Kruckenberg et al., 2011; Betka and Klepeis, 2013) and numerical studies (Beaumont et al., 2004; Jamieson et al., 2007) on exhumed migmatite-granite complexes have concluded that, in order to make crust flow at orogenic scales, three fundamental prerequisites should be met: (1) high temperature, (2) a driving force, and (3) a flow channel. In collisional orogens, high-temperature conditions are commonly induced by crustal thickening (Jamieson et al., 2002, 2004). In this case, crustal flow is commonly triggered by lithostatic pressure gradient from the thickened crust to non-thickened regions (horizontal channel flow) or by gravitational upwelling (vertical flow) due to inverted densities (Whitney et al., 2004). While crustal flow in collisional orogenic systems has attracted much attention, this process has been less frequently described in accretionary orogenic systems (see Collins, 2002; Hyndman et al., 2005; Broussolle et al., 2015; Jiang et al., 2016; Farias et al., 2020). Anatexis in accretionary orogens where crustal thickening is moderate or even negligible points to anomalous thermal regimes. This thermal anomaly is commonly thought to be due to upwelling of hot asthenospheric mantle resulting from lithospheric thinning above subduction systems (Currie et al., 2004; Hyndman et al., 2005), subduction of an active spreading oceanic ridge (Karsten et al., 1996; Polat et al., 2005; Kerrich and Polat, 2006; Cole and Stewart, 2009), or slab break off (Van de Zedde and Wortel, 2001; Mahéo et al., 2002). However, the geodynamic evolution in Chinese Altai is more complex than these models derived from geophysical and geochemical studies.

On the basis of structural and petrological observations, Jiang et al. (2019) proposed the Silurian–Devonian tectonics of the Altai Orogenic Belt could be outlined by tectonic switching from Late Silurian–Early Devonian compression to Middle Devonian extension and back to Late Devonian compression. Our current findings suggest that a 420−410 Ma crustal extension was followed by a 410−390 Ma shortening event, resulting in the D2 folding (Fig. 15). It is noteworthy that such tectonic switching mimics the typical evolution of Pacific-type accretionary orogens, as best exemplified by the Lachlan Orogen in SE Australia, which was interpreted to be a response to variations of subduction dynamics and slab advance and retreat (Collins, 2002; Collins and Richards, 2008).

Thinning of the Altai crust associated with asthenospheric mantle upwelling might have provided efficient heat flux and trigger large-scale anatexis of fertile sediments at the lower crustal level (Jiang et al., 2019) as it is common in other accretionary orogens (e.g., Lachlan fold belt, or Famatinian Orogen, references also to Collins, 2002 and Farias et al., 2020). As argued previously, the switch from horizontal thinning to horizontal shortening drove anatectic melt accumulation in the hinge zones of F2 antiforms, which contributed to amplifying the folds by both weakening the hinge zones and adding buoyancy that led to a generalized upward magma flow. In this regard, the interplay between anatexis and deformation controlled the nature of crustal flow and magma migration, and therefore crustal differentiation in the Chinese Altai. Cyclical slab advance and retreat and switches between shortening and extension in the overriding plate is probably the primary mechanism governing massive generation and migration of crustal magmas, driving mass redistribution and differentiation in long-lasting accretionary orogens in general.

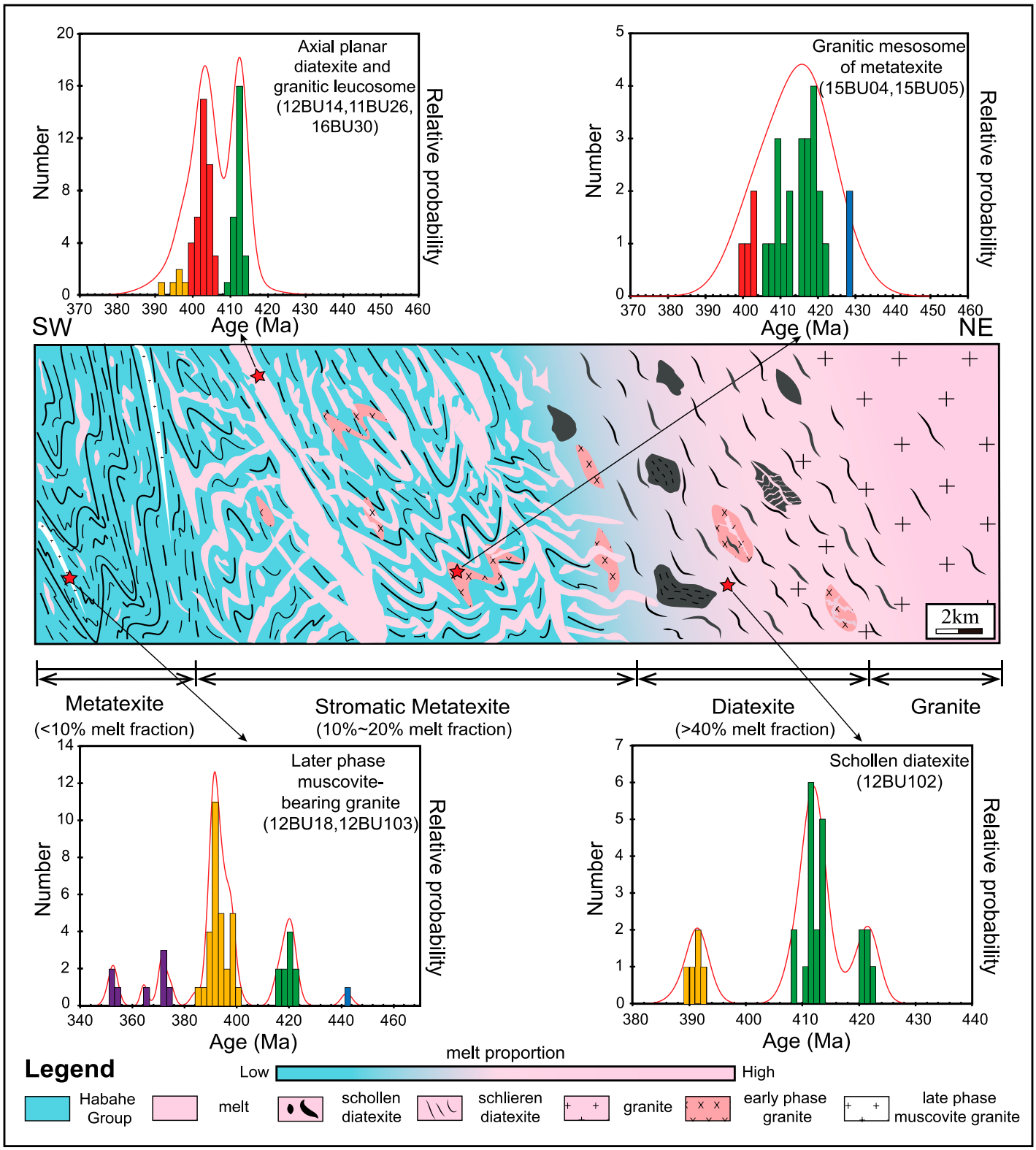

Figure 14. Schematic cross-section of the Tarlang migmatite-granite complex, western Chinese Altai showing zircon U-Pb age spectra of different lithological units. Idealized sample locations are indicated by "stars" and their respective ages are presented in frequency histograms and probability density plots. The main age populations are indicated by different colors in the histograms.

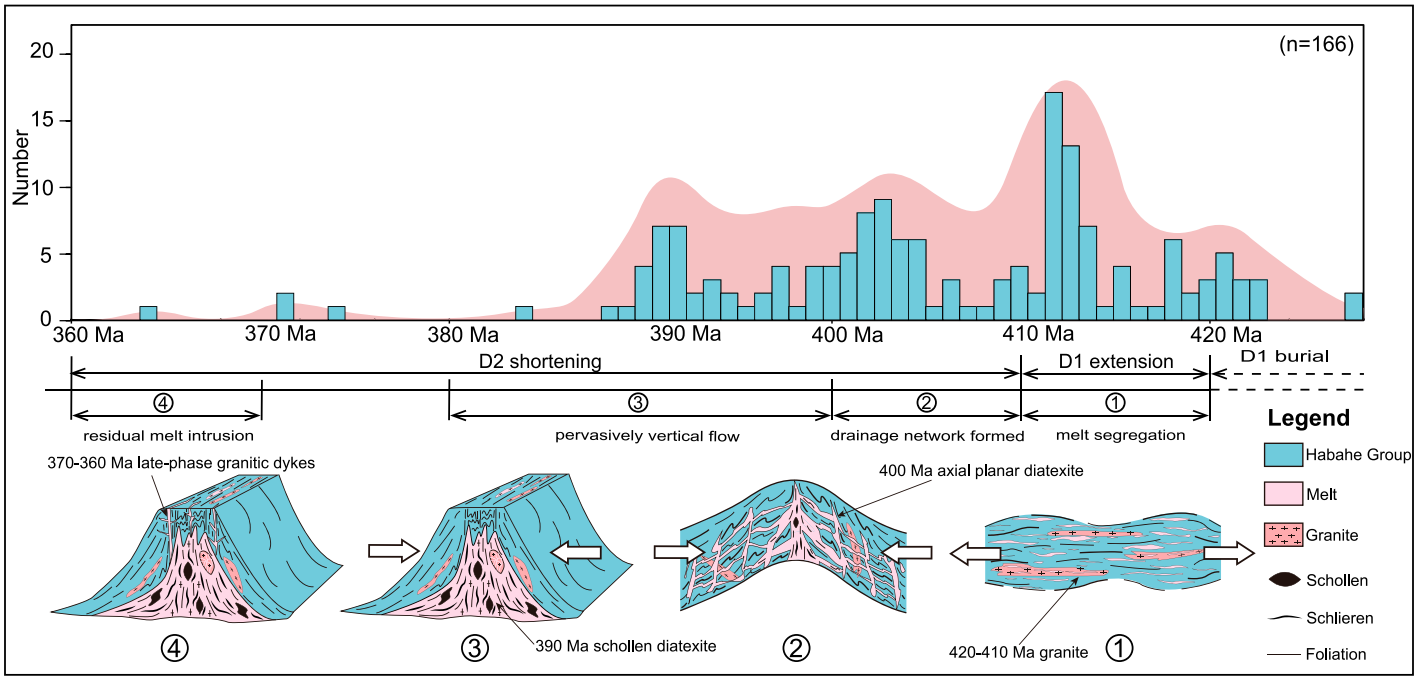

Figure 15. Interpretative temporal and spatial evolution of the Tarlang migmatite-granite complex, western Chinese Altai in the Devonian. Four main stages are outlined: (1) Stage 1 (420–410 Ma): crustal thinning associated with vertical shortening, causes deep crust anatexis and forms stromatic migmatites with sub-horizontal leucosomes; (2) Stage 2 (410–400 Ma): formation of magma network during the early phase of D2 shortening; migmatite starts to lose its coherence and marks the beginning of magma migration and accumulation; (3) Stage 3 (400–380 Ma): development of D2 upright folding, possibly accompanied by buoyant uplift, giving rise to large antiforms where magma accumulates; (4) Stage 4 (370–360 Ma): residual melts intrude into the surrounding metamorphic envelope (un-molten Habahe Group rocks) during the waning stage of anatexis.

6. CONCLUSIONS

Structural and geochronological data allowed us to constrain the geometry, processes, and time scales of flow of the molten orogenic lower crust in the Chinese Altai as it formed the Tarlang migmatite-granite complex. The principal conclusions are:

(1) Migration of magma in the Tarlang migmatite-granite complex occurred in two main stages: (1) deep crust anatexis associated with crustal extension gave rise to the segregation of melt into the S1-parallel sub-horizontal bands; (2) D2 upright folding associated with melt migration, accumulation, and vertical flow transported anatectic magma from orogenic lower to upper crustal levels.

(2) Zircon U-Pb geochronology indicates that syn-extensional, crustal anatexis, and melt segregation took place from ca. 420–410 Ma. Onset of D2 upright folding due to crustal shortening led to magma accumulation in fold hinges and migration when the magma drainage network matured at 410−400 Ma. Soon after, bulk flow of anatectic magmas filled in the cores of regional F2 antiforms until at least 390 Ma, after the molten orogenic lower crust lost its solid framework. The migration of magmas and emplacement of anatectic magmas terminated at ca. 370−360 Ma when the migmatite-granite complex cooled and remaining magmas were emplaced as dykes.

(3) Devonian anatexis, assisted by deformation, governed first the horizontal and then the vertical flow of partially molten orogenic lower crust in the Chinese Altai. Variations in subduction dynamics between slab advance and retreat could be the primary factor governing crustal flow, mass redistribution, and crustal differentiation in Pacific-type supra-subduction systems in general.

ACKNOWLEDGMENTS

This study was supported by the National Natural Science Foundation of China (41672056, 42022017, 42021002, and 41872222), the National Key Research and Development Program of China (grant no. 2017YFC0601205), Strategic Priority Research Program (B) of the Chinese Academy of Sciences (XDB18020203) and the International Partnership Program of the Chinese Academy of Sciences (132744KYSB20190039, 132744KYSB20200001). A Guangdong Special Support Program to Y.D. Jiang and the Thousand Youth Talents Plan to P.F. Li are also acknowledged. The Czech Science Foundation (GACR grant EXPRO 19-27682X) is acknowledged. This is contribution No.IS-2974 from GIGCAS. Constructive reviews from Benito Ábalos and two anonymous reviewers resulted in significant improvements to the paper.

REFERENCES CITED

Allen, M., Alsop, G., and Zhemchuzhnikov, V., 2001, Dome and basin refolding and transpressive inversion along the Karatau Fault System, southern Kazakstan: Journal of the Geological Society, v. 158, no. 1, p. 83–95, https://doi.org/10.1144/jgs.158.1.83.

Beaumont, C., Jamieson, R.A., Nguyen, M.H., and Lee, B., 2001, Himalayan tectonics explained by extrusion of a low-viscosity crustal channel coupled to focused surface denudation: Nature, v. 414, no. 6865, p. 738–742, https://doi.org/10.1038/414738a.

Beaumont, C., Jamieson, R.A., Nguyen, M.H., and Medvedev, S., 2004, Crustal channel flows: 1. Numerical models with applications to the tectonics of the Himalayan-Tibetan orogen: Journal of Geophysical Research. Solid Earth, v. 109, no. B6, https://doi.org/10.1029/2003jb002809.

Betka, P.M., and Klepeis, K.A., 2013, Three-stage evolution of lower crustal gneiss domes at Breaksea Entrance, Fiordland, New Zealand: Tectonics, v. 32, no. 5, p. 1084–1106, https://doi.org/10.1002/tect.20068.

Briggs, S.M., Yin, A., Manning, C.E., Chen, Z.L., Wang, X.F., and Grove, M., 2007, Late Paleozoic tectonic history of the Ertix Fault in the Chinese Altai and its implications for the development of the Central Asian Orogenic System: Geological Society of America Bulletin, v. 119, no. 7−8, p. 944–960, https://doi.org/10.1130/B26044.1.

Briggs, S.M., Yin, A., Manning, C.E., Chen, Z.L., and Wang, X.F., 2009, Tectonic development of the southern Chinese Altai Range as determined by structural geology, thermobarometry, 40Ar/39Ar thermochronology, and

Th/Pb ion-microprobe monazite geochronology: Geological Society of America Bulletin, v. 121, no. 9–10, p. 1381–1393, https://doi.org/10.1130/B26385.1.

Broussolle, A., Štípská, P., Lehmann, J., Schulmann, K., Hacker, B.R., Holder, R., Kylander-Clark, A.R.C., Hanžl, P., Racek, M., Hasalová, P., Lexa, O., Hrdličková, K., and Buriánek, D., 2015, P-T-t-D record of crustal-scale horizontal flow and magma-assisted doming in the SW Mongolian Altai: Journal of Metamorphic Geology, v. 33, no. 4, p. 359–383, https://doi.org/10.1111/jmg.12124.

Broussolle, A., Aguilar, C., Sun, M., Schulmann, K., Štípská, P., Jiang, Y., Yu, Y., Xiao, W., Wang, S., and Míková, J., 2018, Polycyclic Palaeozoic evolution of accretionary orogenic wedge in the southern Chinese Altai: Evidence from structural relationships and U-Pb geochronology: Lithos, v. 314–315, p. 400–424, https://doi.org/10.1016/j.lithos.2018.06.005.

Broussolle, A., Sun, M., Schulmann, K., Guy, A., Aguilar, C., Štípská, P., Jiang, Y., Yu, Y., and Xiao, W., 2019, Are the Chinese Altai "terranes" the result of juxtaposition of different crustal levels during Late Devonian and Permian orogenesis?: Gondwana Research, v. 66, p. 183–206, https://doi.org/10.1016/j.gr.2018.11.003.

Brown, M., 2009, Metamorphic patterns in orogenic systems and the geological record, *in* Cawood, P.A., and Kröner, A., eds., Earth Accretionary Systems in Space and Time: Geological Society of London Special Publication 318, no. 1, p. 37–74, https://doi.org/10.1144/SP318.2.

Brown, M., 2010, Melting of the continental crust during orogenesis: The thermal, rheological, and compositional consequences of melt transport from lower to upper continental crust: Canadian Journal of Earth Sciences, v. 47, no. 5, p. 655–694, https://doi.org/10.1139/E09-057.

Brun, J.P., 1980, The cluster-ridge pattern of mantled gneiss domes in eastern Finland: Evidence for large-scale gravitational instability of the Proterozoic crust: Earth and Planetary Science Letters, v. 47, no. 3, p. 441–449, https://doi.org/10.1016/0012-821X(80)90032-1.

Buriánek, D., Schulmann, K., Hrdličková, K., Hanžl, P., Janoušek, V., Gerdes, A., and Lexa, O., 2017, Geochemical and geochronological constraints on distinct Early-Neoproterozoic and Cambrian accretionary events along southern margin of the Baydrag Continent in western Mongolia: Gondwana Research, v. 47, p. 200–227, https://doi.org/10.1016/j.gr.2016.09.008.

Buslov, M.M., Fujiwara, Y., Iwata, K., and Semakov, N.N., 2004, Late Paleozoic-Early Mesozoic geodynamics of Central Asia: Gondwana Research, v. 7, no. 3, p. 791–808, https://doi.org/10.1016/S1342-937X(05)71064-9.

Cai, K.D., Sun, M., Yuan, C., Zhao, G.C., Xiao, W.J., Long, X.P., and Wu, F.Y., 2011a, Geochronology, petrogenesis and tectonic significance of peraluminous granites from the Chinese Altai, NW China: Lithos, v. 127, no. 1–2, p. 261–281, https://doi.org/10.1016/j.lithos.2011.09.001.

Cai, K.D., Sun, M., Yuan, C., Zhao, G.C., Xiao, W.J., Long, X.P., and Wu, F.Y., 2011b, Prolonged magmatism, juvenile nature and tectonic evolution of the Chinese Altai, NW China: Evidence from zircon U-Pb and Hf isotopic study of Paleozoic granitoids: Journal of Asian Earth Sciences, v. 42, no. 5, p. 949–968, https://doi.org/10.1016/j.jseaes.2010.11.020.

Cavalcante, C., Hollanda, M.H., Vauchez, A., and Kawata, M., 2018, How long can the middle crust remain partially molten during orogeny?: Geology, v. 46, no. 10, p. 839–842, https://doi.org/10.1130/G45126.1.

Chai, F., Mao, J., Dong, L., Yang, F., Liu, F., Geng, X., and Zhang, Z., 2009, Geochronology of metarhyolites from the Kangbutiebao Formation in the Kelang basin, Altay Mountains, Xinjiang: Implications for the tectonic evolution and metallogeny: Gondwana Research, v. 16, no. 2, p. 189–200, https://doi.org/10.1016/j.gr.2009.03.002.

Chen, B., and Jahn, B.M., 2002, Geochemical and isotopic studies of the sedimentary and granitic rocks of the Altai orogen of northwest China and their tectonic implications: Geological Magazine, v. 139, no. 01, p. 1–13, https://doi.org/10.1017/S0016756801006100.

Christensen, N.I., and Mooney, W.D., 1995, Seismic velocity structure and composition of the continental crust: A global view: Journal of Geophysical Research. Solid Earth, v. 100, p. 9761–9788, https://doi.org/10.1029/95JB00259.

Clark, M.K., and Royden, L.H., 2000, Topographic ooze: Building the eastern margin of Tibet by lower crustal flow: Geology, v. 28, no. 8, p. 703–706, https://doi.org/10.1130/0091-7613(2000)28<703:TOBTEM>2.0.CO;2.

Clos, F., Weinberg, R.F., Zibra, I., and Fenwick, M.J., 2019, Archean diapirism recorded by vertical sheath folds in the core of the Yalgoo Dome, Yilgarn Craton: Precambrian Research, v. 320, p. 391–402, https://doi.org/10.1016/j.precamres.2018.11.010.

Cole, R.B., and Stewart, B.W.J.T., 2009, Continental margin volcanism at sites of spreading ridge subduction: Examples from southern Alaska and western California: Tectonophysics, v. 464, no. 1–4, p. 118–136, https://doi.org/10.1016/j.tecto.2007.12.005.

Coleman, R.G., 1989, Continental growth of northwest China: Tectonics, v. 8, no. 3, p. 621–635, https://doi.org/10.1029/TC008i003p00621.

Collins, W.J., 2002, Hot orogens, tectonic switching, and creation of continental crust: Geology, v. 30, no. 6, p. 535–538, https://doi.org/10.1130/0091-7613(2002)030<0535:HOTSAC>2.0.CO;2.

Collins, W.J., and Richards, S.W., 2008, Geodynamic significance of S-type granites in circum-Pacific orogens: Geology, v. 36, no. 7, p. 559–562, https://doi.org/10.1130/G24658A.1.

Coward, M.P., 1981, Diapirism and gravity tectonics: Report of a Tectonic Studies Group conference held at Leeds University, 25–26 March 1980: Journal of Structural Geology, v. 3, no. 1, p. 89–95, https://doi.org/10.1016/0191-8141(81)90059-6.

Cruden, A.R., 1988, Deformation around a rising diapir modeled by creeping flow past a sphere: Tectonics, v. 7, no. 5, p. 1091–1101, https://doi.org/10.1029/TC007i005p01091.

Cui, X., Sun, M., Zhao, G., Yao, J., Zhang, Y., Han, Y., and Dai, L., 2020, A Devonian arc–back-arc basin system in the southern Chinese Altai: Constraints from geochemical and Sr-Nd-Pb isotopic data for meta-basaltic rocks: Lithos, v. 366–367, no. 105540, https://doi.org/10.1016/j.lithos.2020.105540.

Currie, C., Wang, K., Hyndman, R.D., He, J.J.E., and Letters, P.S., 2004, The thermal effects of steady-state slab-driven mantle flow above a subducting plate: The Cascadia subduction zone and backarc: Earth and Planetary Science Letters, v. 223, no. 1–2, p. 35–48, https://doi.org/10.1016/j.epsl.2004.04.020.

Demoux, A., Kröner, A., Badarch, G., Jian, P., Tomurhuu, D., and Wingate, M.T.D., 2009, Zircon ages from the Baydrag Block and the Bayankhongor Ophiolite Zone: Time constraints on late Neoproterozoic to Cambrian subduction-and accretion-related magmatism in central Mongolia: The Journal of Geology, v. 117, no. 4, p. 377–397, https://doi.org/10.1086/598947.

Dixon, J.M., 1975, Finite strain and progressive deformation in models of diapiric structures: Tectonophysics, v. 28, no. 1–2, p. 89–124, https://doi.org/10.1016/0040-1951(75)90060-8.

Farias, P., Weinberg, R., Sola, A., and Becchio, R., 2020, From crustal thickening to orogen-parallel escape: The 120-myr-long HT-LP evolution recorded by titanite in the Paleozoic Famatinian backarc, NW Argentina: Tectonics, v. 39, no. 9, https://doi.org/10.1029/2020tc006184.

Faure, M., Lalevée, F., Gusokujima, Y., Iiyama, J.T., and Cadet, J.P., 1986, The pre-Cretaceous deep-seated tectonics of the Abukuma massif and its place in the structural framework of Japan: Earth and Planetary Science Letters, v. 77, no. 3, p. 384–398, https://doi.org/10.1016/0012-821X(86)90148-2.

Fowler, T., and Osman, A., 2001, Gneiss-cored interference dome associated with two phases of late Pan-African thrusting in the central Eastern Desert, Egypt: Precambrian Research, v. 108, no. 1–2, p. 17–43, https://doi.org/10.1016/S0301-9268(00)00146-7.

Gates, A.E., 1987, Transpressional dome formation in the Southwest Virginia Piedmont: American Journal of Science, v. 287, no. 9, p. 927–949, https://doi.org/10.2475/ajs.287.9.927.

Gervais, F., Brown, R.L., and Crowley, J.L., 2010, Tectonic implications for a Cordilleran orogenic base in the Frenchman Cap dome, southeastern Canadian Cordillera: Journal of Structural Geology, v. 32, no. 7, p. 941–959, https://doi.org/10.1016/j.jsg.2010.05.006.

Guo, X.J., Li, Y., Kong, L.H., Zheng, J.H., and Sun, D.Q., 2015, Geological characteristics and metallogenesis of the Boketubayi iron-manganese deposit in Altay [in Chinese with English abstract]: Xinjiang Geoscience, v. 29, no. 6, p. 1309–1318.

Guy, A., Schulmann, K., Soejono, I., and Xiao, W. J., 2020, Revision of the Chinese Altai-East Junggar Terrane accretion model based on geophysical and geological constraints: Tectonics, v. 39, no. 4, https://doi.org/10.1029/2019tc006026.

Hanžl, P., Schulmann, K., Janoušek, V., Lexa, O., Hrdličková, K., Jiang, Y., Buriánek, D., Altanbaatar, B., Ganchuluun, T., and Erban, V., 2016, Making continental crust: Origin of Devonian orthogneisses from SE Mongolian Altai: Journal of Geosciences (Prague), v. 61, no. 1, p. 25–50, https://doi.org/10.3190/jgeosci.206.

Holtzman, B.K., Kohlstedt, D.L., and Morgan, J.P., 2005, Viscous energy dissipation and strain partitioning in partially molten rocks: Journal of Petrology, v. 46, no. 12, p. 2569–2592, https://doi.org/10.1093/petrology/egi065.

Hu, W.W., Li, P.F., Rosenbaum, G., Liu, J.L., Jourdan, F., Jiang, Y.D., Wu, D., Zhang, J., Yuan, C., and Sun, M., 2020, Structural evolution of the eastern segment of the Irtysh Shear Zone: Implications for the collision between the East Junggar Terrane and the Chinese Altai Orogen (northwestern China): Journal of Structural Geology, v. 139, no. 104126, https://doi.org/10.1016/j.jsg.2020.104126.

Huang, Y.Q., Jiang, Y., Yu, Y., Collett, S., Wang, S., Shu, T., and Xu, K., 2020a, Nd-Hf isotopic decoupling of the Silurian–Devonian granitoids in the Chinese Altai: A consequence of crustal recycling of the Ordovician accretionary wedge?: Journal of Earth Science, v. 31, p. 102–114, https://doi.org/10.1007/s12583-019-1217-x.

Huang, Y.Q., Jiang, Y., Collett, S., Wang, S., Xu, K., Shu, T., Li, P., and Yuan, C., 2020b, Magmatic recycling of accretionary wedge: A new perspective on Silurian-Devonian I-type granitoids generation in the Chinese Altai: Gondwana Research, v. 78, p. 291–307, https://doi.org/10.1016/j.gr.2019.07.019.

Hyndman, R.D., Currie, C.A., and Mazzotti, S., 2005, Subduction zone backarcs, continental mobiles, and orogenic heat: GSA Today, v. 15, no. 2, p. 4–10, https://doi.org/10.1130/1052-5173(2005)015<4:SZBMBA>2.0.CO;2.

Ireland, T.R., and Williams, I.S., 2003, Considerations in zircon geochronology by SIMS: Reviews in Mineralogy and Geochemistry, v. 53, no. 1, p. 215–241, https://doi.org/10.2113/0530215.

Jamieson, R.A., Beaumont, C., Nguyen, M., and Lee, B., 2002, Interaction of metamorphism, deformation and exhumation in large convergent orogens: Journal of Metamorphic Geology, v. 20, no. 1, p. 9–24, https://doi.org/10.1046/j.0263-4929.2001.00357.x.

Jamieson, R.A., Beaumont, C., Medvedev, S., and Nguyen, M.H., 2004, Crustal channel flows: 2. Numerical models with implications for metamorphism in the Himalayan-Tibetan orogen: Journal of Geophysical Research. Solid Earth, v. 109, no. B6, p. 1–24, https://doi.org/10.1029/2003jb002811.

Jamieson, R.A., Beaumont, C., Nguyen, M.H., and Culshaw, N.G., 2007, Synconvergent ductile flow in variable-strength continental crust: Numerical models with application to the western Grenville orogen: Tectonics, v. 26, no. 5, p. 1–23, https://doi.org/10.1029/2006TC002036.

Jamieson, R.A., Unsworth, M.J., Harris, N.B.W., Rosenberg, C.L., and Schulmann, K., 2011, Crustal Melting and the Flow of Mountains: Elements, v. 7, no. 4, p. 253–260, https://doi.org/10.2113/gselements.7.4.253.

Janoušek, V., Jiang, Y., Buriánek, D., Schulmann, K., Hanžl, P., Soejono, I., Kröner, A., Altanbaatar, B., Erban, V., Lexa, O., Ganchuluun, T., and Košler, J., 2018, Cambrian–Ordovician magmatism of the Ikh-Mongol Arc System exemplified by the Khantaishir Magmatic Complex (Lake Zone, south–central Mongolia): Gondwana

Research, v. 54, p. 122–149, https://doi.org/10.1016/j.gr.2017.10.003.

Jiang, Y.D., Sun, M., Zhao, G.C., Yuan, C., Xiao, W.J., Xia, X.P., Long, X.P., and Wu, F.Y., 2010, The similar to 390 Ma high-T metamorphic event in the Chinese Altai: A consequence of ridge-subduction?: American Journal of Science, v. 310, no. 10, p. 1421–1452, https://doi.org/10.2475/10.2010.08.

Jiang, Y.D., Sun, M., Zhao, G.C., Yuan, C., Xiao, W.J., Xia, X.P., Long, X.P., and Wu, F.Y., 2011, Precambrian detrital zircons in the Early Paleozoic Chinese Altai: Their provenance and implications for the crustal growth of central Asia: Precambrian Research, v. 189, no. 1–2, p. 140–154, https://doi.org/10.1016/j.precamres.2011.05.008.

Jiang, Y.D., Štípská, P., Sun, M., Schulmann, K., Zhang, J., Wu, Q.H., Long, X.P., Yuan, C., Racek, M., Zhao, G.C., and Xiao, W.J., 2015, Juxtaposition of Barrovian and migmatite domains in the Chinese Altai: A result of crustal thickening followed by doming of partially molten lower crust: Journal of Metamorphic Geology, v. 33, no. 1, p. 45–70, https://doi.org/10.1111/jmg.12110.

Jiang, Y.D., Schulmann, K., Sun, M., Štípská, P., Guy, A., Janoušek, V., Lexa, O., and Yuan, C., 2016, Anatexis of accretionary wedge, Pacific-type magmatism, and formation of vertically stratified continental crust in the Altai Orogenic Belt: Tectonics, v. 35, no. 12, p. 3095–3118, https://doi.org/10.1002/2016TC004271.

Jiang, Y.D., Schulmann, K., Kröner, A., Sun, M., Lexa, O., Janoušek, V., Buriánek, D., Yuan, C., and Hanžl, P., 2017, Neoproterozoic-Early Paleozoic peri-Pacific accretionary evolution of the Mongolian Collage System: Insights from geochemical and U-Pb zircon data from the Ordovician sedimentary wedge in the Mongolian Altai: Tectonics, v. 36, no. 11, p. 2305–2331, https://doi.org/10.1002/2017TC004533.

Jiang, Y.D., Schulmann, K., Sun, M., Weinberg, R.F., Štípská, P., Li, P.F., Zhang, J., Chopin, F., Wang, S., Xia, X.P., and Xiao, W.J., 2019, Structural and geochronological constraints on Devonian suprasubduction tectonic switching and Permian collisional dynamics in the Chinese Altai, Central Asia: Tectonics, v. 38, no. 1, p. 253–280, https://doi.org/10.1029/2018TC005231.

Kang, D.Y., Zhang, Z.M., Palin, R.M., Tian, Z.L., and Dong, X., 2020, Prolonged partial melting of garnet amphibolite from the eastern Himalayan syntaxis: Implications for the tectonic evolution of large hot orogens: Journal of Geophysical Research. Solid Earth, v. 125, no. 6, https://doi.org/10.1029/2019JB019119.

Karsten, J., Klein, E., and Sherman, S.J.L., 1996, Subduction zone geochemical characteristics in ocean ridge basalts from the southern Chile Ridge: Implications of modern ridge subduction systems for the Archean: Lithos, v. 37, no. 2−3, p. 143–161, https://doi.org/10.1016/0024-4937(95)00034-8.

Kerrich, R., and Polat, A.J.T., 2006, Archean greenstone-tonalite duality: Thermochemical mantle convection models or plate tectonics in the early Earth global dynamics: Tectonophysics, v. 415, no. 1−4, p. 141–165, https://doi.org/10.1016/j.tecto.2005.12.004.

Kratinová, Z., Závada, P., Hrouda, F., and Schulmann, K., 2006, Non-scaled analogue modelling of AMS development during viscous flow: a simulation on diapir-like structures: Tectonophysics, v. 418, no. 1–2, p. 51–61, https://doi.org/10.1016/j.tecto.2005.12.013.

Kruckenberg, S.C., Vanderhaeghe, O., Ferré, E.C., Teyssier, C., and Whitney, D.L., 2011, Flow of partially molten crust and the internal dynamics of a migmatite dome, Naxos, Greece: Tectonics, v. 30, no. 3, https://doi.org/10.1029/2010TC002751.

Labrousse, L., Duretz, T., and Gerya, T., 2015, H2O-fluid-saturated melting of subducted continental crust facilitates exhumation of ultrahigh-pressure rocks in continental subduction zones: Earth and Planetary Science Letters, v. 428, p. 151–161, https://doi.org/10.1016/j.epsl.2015.06.016.

Laurent-Charvet, S., Charvet, J., Monié, P., and Shu, L., 2003, Late Paleozoic strike-slip shear zones in eastern Central Asia (NW China): New structural and geochronological data: Tectonics, v. 22, no. 2, https://doi.org/10.1029/2001TC901047.

Lehmann, J., Schulmann, K., Lexa, O., Corsini, M., Kröner, A., Štípská, P., Tomurhuu, D., and Otgonbator, D., 2010, Structural constraints on the evolution of the Central Asian Orogenic Belt in SW Mongolia: American Journal of Science, v. 310, no. 7, p. 575–628, https://doi.org/10.2475/07.2010.02.

Lehmann, J., Schulmann, K., Lexa, O., Závada, P., Štípská, P., Hasalová, P., Belyanin, G., and Corsini, M., 2017, Detachment folding of partially molten crust in accretionary orogens: A new magma-enhanced vertical mass and heat transfer mechanism: Lithosphere, v. 9, p. 889–909, https://doi.org/10.1130/L670.1.

Le Pichon, X., Henry, P., and Goffé, B., 1997, Uplift of Tibet: From eclogites to granulites—implications for the Andean Plateau and the Variscan belt: Tectonophysics, v. 273, no. 1, p. 57–76, https://doi.org/10.1016/S0040-1951(96)00288-0.

Li, C.Y., Zhang, H., Wang, F.Y., Liu, J.Q., Sun, Y.L., Hao, X.L., Li, Y.L., and Sun, W., 2012, The formation of the Dabaoshan porphyry molybdenum deposit induced by slab rollback: Lithos, v. 150, p. 101–110, https://doi.org/10.1016/j.lithos.2012.04.001.

Li, P.F., Sun, M., Rosenbaum, G., Cai, K.D., and Yu, Y., 2015a, Structural evolution of the Irtysh Shear Zone (northwestern China) and implications for the amalgamation of arc systems in the Central Asian Orogenic Belt: Journal of Structural Geology, v. 80, p. 142–156, https://doi.org/10.1016/j.jsg.2015.08.008.

Li, P.F., Yuan, C., Sun, M., Long, X.P., and Cai, K.D., 2015b, Thermochronological constraints on the late Paleozoic tectonic evolution of the southern Chinese Altai: Journal of Asian Earth Sciences, v. 113, p. 51–60, https://doi.org/10.1016/j.jseaes.2014.11.004.

Li, P.F., Sun, M., Rosenbaum, G., Jiang, Y., and Cai, K., 2016, Structural evolution of zonal metamorphic sequences in the southern Chinese Altai and relationships to Permian transpressional tectonics in the Central Asian Orogenic Belt: Tectonophysics, v. 693, p. 277–289, https://doi.org/10.1016/j.tecto.2015.11.035.

Li, P.F., Sun, M., Rosenbaum, G., Jourdan, F., Li, S., and Cai, K., 2017, Late Paleozoic closure of the Ob-Zaisan Ocean along the Irtysh shear zone (NW China): Implications for arc amalgamation and oroclinal bending in the Central Asian orogenic belt: Geological Society of America Bulletin, v. 129, p. 547–569, https://doi.org/10.1130/B31541.1.

Li, P.F., Sun, M., Shu, C.T., Yuan, C., Jiang, Y.D., Zhang, L., and Cai, K.D., 2019, Evolution of the Central Asian Orogenic Belt along the Siberian margin from Neoproterozoic-Early Paleozoic accretion to Devonian trench retreat and a comparison with Phanerozoic eastern Australia: Earth-Science Reviews, v. 198, no. 102951, https://doi.org/10.1016/j.earscirev.2019.102951.

Li, X.H., Liu, Y., Li, Q.L., Guo, C.H., and Chamberlain, K.R., 2009, Correction to "Precise determination of Phanerozoic zircon Pb/Pb age by multicollector SIMS without external standardization": Geochemistry, Geophysics, Geosystems, v. 10, no. 6, p. 573–575, https://doi.org/10.1029/2009GC002607.

Li, Z.L., Yang, X.Q., Li, Y., Santosh, M., Chen, H., and Xiao, W.J., 2014, Late Paleozoic tectono–metamorphic evolution of the Altai segment of the Central Asian Orogenic Belt: Constraints from metamorphic P–T pseudosection and zircon U–Pb dating of ultra-high-temperature granulite: Lithos, v. 204, p. 83–96, https://doi.org/10.1016/j.lithos.2014.05.022.

Liu, W., Liu, L.J., Liu, X.J., Shang, H.J., and Zhou, G., 2010, Age of the Early Devonian Kangbutiebao Formation along the southern Altay Mountains and its northeastern extension [in Chinese with English abstract]: Yanshi Xuebao, v. 26, no. 2, p. 387–400.

Liu, W., Liu, X.J., and Xiao, W.J., 2012, Massive granitoid production without massive continental-crust growth in the Chinese Altay: Insight into the source rock of granitoids using integrated zircon U-Pb age, Hf-Nd-Sr isotopes and geochemistry: American Journal of Science, v. 312, no. 6, p. 629–684, https://doi.org/10.2475/06.2012.02.

Liu, Y., Hu, Z., Gao, S., Günther, D., Xu, J., Gao, C., and Chen, H., 2008, In situ analysis of major and trace elements of anhydrous minerals by LA-ICP-MS without applying an internal standard: Chemical Geology, v. 257, no. 1–2, p. 34–43, https://doi.org/10.1016/j.chemgeo.2008.08.004.

Liu, Z., Bartoli, O., Tong, L., Xu, Y.G., and Huang, X., 2020, Permian ultrahigh–temperature reworking in the southern Chinese Altai: Evidence from petrology, P–T estimates, zircon and monazite U–Th–Pb geochronology: Gondwana Research, v. 78, p. 20–40, https://doi.org/10.1016/j.gr.2019.08.007.

Long, X.P., Sun, M., Yuan, C., Xiao, W.J., and Cai, K.D., 2008, Early Paleozoic sedimentary record of the Chinese Altai: Implications for its tectonic evolution: Sedimentary Geology, v. 208, no. 3−4, p. 88–100, https://doi.org/10.1016/j.sedgeo.2008.05.002.

Long, X.P., Yuan, C., Sun, M., Xiao, W.J., Zhao, G.C., Wang, Y.J., Cai, K.D., Xia, X.P., and Xie, L.W., 2010, Detrital zircon ages and Hf isotopes of the early Paleozoic flysch sequence in the Chinese Altai, NW China: New constrains on depositional age, provenance and tectonic evolution: Tectonophysics, v. 480, p. 213–231, https://doi.org/10.1016/j.tecto.2009.10.013.

Ludwig, K.R., 2003, User's Manual for Isoplot 3.00, A Geochronological Toolkit for Microsoft Excel: Berkeley Geochronology Center Special Publication, v. 4, 70 p.

Mahéo, G., Guillot, S., Blichert-Toft, J., Rolland, Y., Pêcher, A.J.E., and Letters, P.S., 2002, A slab breakoff model for the Neogene thermal evolution of South Karakorum and South Tibet: Earth and Planetary Science Letters, v. 195, no. 1−2, p. 45–58, https://doi.org/10.1016/S0012-821X(01)00578-7.

Maierová, P., Lexa, O., Schulmann, K., and Štípská, P., 2014, Contrasting tectono-metamorphic evolution of orogenic lower crust in the Bohemian Massif: A numerical model: Gondwana Research, v. 25, no. 2, p. 509–521, https://doi.org/10.1016/j.gr.2012.08.020.

Martini, A., Bitencourt, M.F., Weinberg, R.F., and De Toni, G.B., 2019a, Melt-collecting structures and the formation of extraction dykes during syntectonic anatexis of the Camboriú Complex, south Brazil: Journal of Structural Geology, v. 127, no. 103866, https://doi.org/10.1016/j.jsg.2019.103866.

Martini, A., Bitencourt, M.d.F., Weinberg, R. F., De Toni, G.B., and Lauro, V.S.N., 2019b, From migmatite to magma: Crustal melting and generation of granite in the Camboriú Complex, south Brazil: Lithos, v. 340−341, p. 270−286, https://doi.org/10.1016/j.lithos.2019.05.017.

Nelson, K.D., et al., 1996, Partially molten middle crust beneath southern Tibet: Synthesis of project INDEPTH results: Science, v. 274, no. 5293, p. 1684–1688, https://doi.org/10.1126/science.274.5293.1684.

Norlander, B.H., Whitney, D.L., Teyssier, C., and Vanderhaeghe, O., 2002, Partial melting and decompression of the Thor-Odin dome, Shuswap metamorphic core complex, Canadian Cordillera: Lithos, v. 61, no. 3, p. 103–125, https://doi.org/10.1016/S0024-4937(02)00075-0.

Paterson, S.R., Vernon, R.H., and Tobisch, O., 1989, A review of criteria for the identification of magmatic and tectonic foliations in granitoids: Journal of Structural Geology, v. 11, no. 3, p. 349–363, https://doi.org/10.1016/0191-8141(89)90074-6.

Polat, A., Kusky, T., Li, J., Fryer, B., Kerrich, R., and Patrick, K., 2005, Geochemistry of Neoarchean (ca. 2.55–2.50 Ga) volcanic and ophiolitic rocks in the Wutaishan greenstone belt, central orogenic belt, North China craton: Implications for geodynamic setting and continental growth: Geological Society of America Bulletin, v. 117, no. 11−12, p. 1387–1399, https://doi.org/10.1130/B25724.1.

Qu, G.S., and Zhang, J.J., 1994, Oblique thrust systems in the Altay orogen, China: Journal of Southeast Asian Earth Sciences, v. 9, no. 3, p. 277–287, https://doi.org/10.1016/0743-9547(94)90035-3.

Ramberg, H., 1980, Diapirism and gravity collapse in the Scandinavian Caledonides: Journal of the Geological Society, v. 137, no. 5, p. 261–270, https://doi.org/10.1144/gsjgs.137.3.0261.

Rosenberg, C., and Handy, M., 2005, Experimental deformation of partially melted granite revisited: Implications for the continental crust: Journal of Metamorphic Geology, v. 23, no. 1, p. 19–28, https://doi.org/10.1111/j.1525-1314.2005.00555.x.

Royden, L.H., Burchfiel, B.C., and van der Hilst, R.D., 2008, The geological evolution of the Tibetan Plateau: Science, v. 321, no. 5892, p. 1054–1058, https://doi.org/10.1126/science.1155371.

Rutter, E.H., and Neumann, D.H.K., 1995, Experimental deformation of partially molten Westerly granite under fluid-absent conditions, with implications for the extraction of granitic magmas: Journal of Geophysical Research. Solid Earth, v. 100, no. B8, p. 15697–15715, https://doi.org/10.1029/94JB03388.

Sawyer, E.W., 1994, Melt segregation in the continental crust: Geology, v. 22, no. 11, p. 1019–1022, https://doi.org/10.1130/0091-7613(1994)022<1019:MSITCC>2.3.CO;2.

Sawyer, E.W., 1996, Melt segregation and magma flow in migmatites: Implications for the generation of granite magmas: Transactions of the Royal Society of Edinburgh. Earth Sciences, v. 87, no. 1–2, p. 85–94, https://doi.org/10.1017/S0263593300006507.

Sawyer, E.W., 1998, Formation and evolution of granite magmas during crustal reworking: The significance of diatexites: Journal of Petrology, v. 39, no. 6, p. 1147–1167, https://doi.org/10.1093/petroj/39.6.1147.

Sawyer, E.W., 2001, Melt segregation in the continental crust: Distribution and movement of melt in anatectic rocks: Journal of Metamorphic Geology, v. 19, p. 291–309, https://doi.org/10.1046/j.0263-4929.2000.00312.x.

Schofield, D.I., and D'Lemos, R., 1998, Relationships between syn-tectonic granite fabrics and regional PTtd paths: An example from the Gander-Avalon boundary of NE Newfoundland: Journal of Structural Geology, v. 20, no. 4, p. 459–471, https://doi.org/10.1016/S0191-8141(97)00117-X.

Schulmann, K., Lexa, O., Štípská, P., Racek, M., Tajčmanová, L., Konopásek, J., Edel, J.B., Peschler, A., and Lehmann, J., 2008, Vertical extrusion and horizontal channel flow of orogenic lower crust: Key exhumation mechanisms in large hot orogens?: Journal of Metamorphic Geology, v. 26, no. 2, p. 273–297, https://doi.org/10.1111/j.1525-1314.2007.00755.x.

Şengör, A.M.C., Natal'in, B.A., and Burtman, V.S., 1993, Evolution of the Altaid tectonic collage and Paleozoic crustal growth in Eurasia: Nature, v. 364, p. 299–307, https://doi.org/10.1038/364299a0.

Skrzypek, E., Kawakami, T., Hirajima, T., Sakata, S., Hirata, T., and Ikeda, T., 2016, Revisiting the high temperature metamorphic field gradient of the Ryoke Belt (SW Japan): New constraints from the Iwakuni-Yanai area: Lithos, v. 260, p. 9–27, https://doi.org/10.1016/j.lithos.2016.04.025.

Sláma, J., Košler, J., Condon, D.J., Crowley, J.L., Gerdes, A., Hanchar, J.M., Horstwood, M.S., Morris, G.A., Nasdala, L., and Norberg, N., 2008, Plešovice zircon: A new natural reference material for U-Pb and Hf isotopic microanalysis: Chemical Geology, v. 249, no. 1–2, p. 1–35, https://doi.org/10.1016/j.chemgeo.2007.11.005.

Soejono, I., Čáp, P., Míková, J., Janoušek, V., Buriánek, D., and Schulmann, K., 2018, Early Palaeozoic sedimentary record and provenance of flysch sequences in the Hovd Zone (western Mongolia): Implications for the geodynamic evolution of the Altai accretionary wedge system: Gondwana Research, v. 64, p. 163–183, https://doi.org/10.1016/j.gr.2018.07.005.

Stacey, J.t., and Kramers, J., 1975, Approximation of terrestrial lead isotope evolution by a two-stage model: Earth and Planetary Science Letters, v. 26, no. 2, p. 207–221, https://doi.org/10.1016/0012-821X(75)90088-6.

Steenken, A., Siegesmund, S., and Heinrichs, T., 2000, The emplacement of the Rieserferner Pluton (Eastern Alps, Tyrol): Constraints from field observations, magnetic fabrics and microstructures: Journal of Structural Geology, v. 22, no. 11–12, p. 1855–1873, https://doi.org/10.1016/S0191-8141(00)00071-7.

Štípská, P., Schulmann, K., Lehmann, J., Corsini, M., Lexa, O., and Tomurhuu, D., 2010, Early Cambrian eclogites in SW Mongolia: Evidence that the Palaeo-Asian Ocean suture extends further east than expected: Journal of Metamorphic Geology, v. 28, no. 9, p. 915–933, https://doi.org/10.1111/j.1525-1314.2010.00899.x.

Štípská, P., Hasalová, P., Powell, R., Závada, P., Schulmann, K., Racek, M., Aguilar, C., and Chopin, F., 2019, The effect of melt infiltration on metagranitic rocks: The Snieznik dome, Bohemian Massif: Journal of Petrology, v. 60, no. 3, p. 591–618, https://doi.org/10.1093/petrology/egz007.

Sun, M., Yuan, C., Xiao, W.J., Long, X.P., Xia, X.P., Zhao, G.C., Lin, S., Wu, F.Y., and Kröner, A., 2008, Zircon U-Pb and Hf isotopic study of gneissic rocks from the Chinese Altai: Progressive accretionary history in the early to middle Palaeozoic: Chemical Geology, v. 247, no. 3–4, p. 352–383, https://doi.org/10.1016/j.chemgeo.2007.10.026.

Sun, M., Long, X.P., Cai, K.D., Jiang, Y.D., Wang, B., Yuan, C., Zhao, G.C., Xiao, W.J., and Wu, F.Y., 2009, Early Paleozoic ridge subduction in the Chinese Altai: Insight from the abrupt change in zircon Hf isotopic compositions: Science in China. Series D, Earth Sciences, v. 52, no. 9, p. 1345–1358, https://doi.org/10.1007/s11430-009-0110-3.

Symington, N. J., Weinberg, R. F., Hasalová, P., Wolfram, L. C., Raveggi, M., and Armstrong, R. A. J. B., 2014, Multiple intrusions and remelting-remobilization events in a magmatic arc: The St. Peter Suite, South Australia, v. 126, no. 9–10, p. 1200–1218, https://doi.org/10.1130/b30975.1.

Tong, L.X., Xu, Y.G., Cawood, P.A., Zhou, X., Chen, Y.B., and Liu, Z., 2014, Anticlockwise P-T evolution at ~280 Ma recorded from ultrahigh-temperature metapelitic granulite in the Chinese Altai orogenic belt, a possible link with the Tarim mantle plume?: Journal of Asian Earth Sciences, v. 94, p. 1–11, https://doi.org/10.1016/j.jseaes.2014.07.043.

Unsworth, M.J., Jones, A.G., Wei, W., Marquis, G., Gokarn, S.G., Spratt, J.E., and The INDEPTH-MT team, 2005, Crustal rheology of the Himalaya and Southern Tibet inferred from magnetotelluric data: Nature, v. 438, no. 7064, p. 78–81, https://doi.org/10.1038/nature04154.

Uyeda, S., and Miyashiro, A., 1974, Plate tectonics and the Japanese Islands: A synthesis: Geological Society of America Bulletin, v. 85, no. 7, p. 1159–1170, https://doi.org/10.1130/0016-7606(1974)85<1159:PTATJI>2.0.CO;2.

Van de Zedde, D.M.A., and Wortel, M.J.R., 2001, Shallow slab detachment as a transient source of heat at midlithospheric depths: Tectonics, v. 20, no. 6, p. 868–882, https://doi.org/10.1029/2001TC900018.

Vanderhaeghe, O., Medvedev, S., Fullsack, P., Beaumont, C., and Jamieson, R.A., 2003, Evolution of orogenic wedges and continental plateaux: Insights from crustal thermal–mechanical models overlying subducting mantle lithosphere: Geophysical Journal International, v. 153, no. 1, p. 27–51, https://doi.org/10.1046/j.1365-246X.2003.01861.x.

Wan, B., Xiao, W., Zhang, L., Windley, B.F., Han, C., and Quinn, C.D., 2011, Contrasting styles of mineralization in the Chinese Altai and East Junggar, NW China: Implications for the accretionary history of the southern Altaids: Journal of the Geological Society, v. 168, no. 6, p. 1311–1321, https://doi.org/10.1144/0016-76492011-021.

Wang, S., Xu, K., Huang, Y.Q., Kong, L.Z., Qi, Y., Song, S.P., Zhang, J., and Jiang, Y., 2018, Permian deformational history of western Chinese Altai orogenic belt: Insights from structural and monazite U-Pb data [in Chinese with English abstract]: Geotectonica et Metallogenia, v. 42, p. 1–12.

Wang, T., Hong, D.W., Jahn, B.M., Tong, Y., Wang, Y.B., Han, B.F., and Wang, X.X., 2006, Timing, petrogenesis, and setting of Paleozoic synorogenic intrusions from the Altai Mountains, northwest China: Implications for the tectonic evolution of an accretionary orogen: The Journal of Geology, v. 114, no. 6, p. 735–751, https://doi.org/10.1086/507617.

Wang, W., Wei, C.J., Wang, T., Lou, Y.X., and Chu, H., 2009, Confirmation of pelitic granulite in the Altai orogen and its geological significance: Chinese Science Bulletin, v. 54, no. 14, p. 2543–2548, https://doi.org/10.1007/s11434-009-0041-6.

Wei, C., Clarke, G., Tian, W., and Qiu, L., 2007, Transition of metamorphic series from the Kyanite- to andalusite-types in the Altai orogen, Xinjiang, China: Evidence from petrography and calculated KMnFMASH and KFMASH phase relations: Lithos, v. 96, no. 3–4, p. 353–374, https://doi.org/10.1016/j.lithos.2006.11.004.

Weinberg, R.F., and Mark, G., 2008, Magma migration, folding, and disaggregation of migmatites in the Karakoram Shear Zone, Ladakh, NW India: Geological Society of America Bulletin, v. 120, no. 7–8, p. 994–1009, https://doi.org/10.1130/B26227.1.

Weinberg, R.F., Hasalova, P., Ward, L., and Fanning, C.M., 2013, Interaction between deformation and magma extraction in migmatites: Examples from Kangaroo Island, South Australia: Geological Society of America Bulletin, v. 125, no. 7–8, p. 1282–1300, https://doi.org/10.1130/B30781.1.

Weinberg, R.F., Veveakis, E., and Regenauer-Lieb, K., 2015, Compaction-driven melt segregation in migmatites: Geology, v. 43, no. 6, p. 471–474, https://doi.org/10.1130/G36562.1.

Weinberg, R.F., Becchio, R., Farias, P., Suzaño, N., and Sola, A., 2018, Early Paleozoic accretionary orogenies in NW Argentina: Growth of West Gondwana: Earth-Science Reviews, v. 187, p. 219–247, https://doi.org/10.1016/j.earscirev.2018.10.001.

Whitehouse, M.J., Kamber, B.S., and Moorbath, S., 1999, Age significance of U–Th–Pb zircon data from early Archaean rocks of west Greenland—a reassessment based on combined ion-microprobe and imaging studies: Chemical Geology, v. 160, no. 3, p. 201–224, https://doi.org/10.1016/S0009-2541(99)00066-2.

Whitney, D.L., Teyssier, C., and Vanderhaeghe, O., 2004, Gneiss domes and crustal flow, *in* Whitney, D.L., Teyssier, C., and Siddoway, C.S., eds., Gneiss Domes in Orogeny: Geological Society of America Special Paper 380, p. 15–33, https://doi.org/10.1130/0-8137-2380-9.15.

Whitney, D.L., Teyssier, C., Rey, P., and Buck, W.R., 2013, Continental and oceanic core complexes: Geological Society of America Bulletin, v. 125, p. 273–298, https://doi.org/10.1130/B30754.1.

Wiedenbeck, M., Alle, P., Corfu, F., Griffin, W., Meier, M., Oberli, F., Quadt, A., Roddick, J., and Spiegel, W., 1995, Three natural zircon standards for U-Th-Pb, Lu-Hf, trace element and REE analyses: Geostandards Newsletter, v. 19, no. 1, p. 1–23, https://doi.org/10.1111/j.1751-908X.1995.tb00147.x.

Wilhem, C., Windley, B.F., and Stampfli, G.M., 2012, The Altaids of Central Asia: A tectonic and evolutionary innovative review: Earth-Science Reviews, v. 113, no. 3–4, p. 303–341, https://doi.org/10.1016/j.earscirev.2012.04.001.

Windley, B.F., and Xiao, W., 2018, Ridge subduction and slab windows in the Central Asian Orogenic Belt: Tectonic implications for the evolution of an accretionary orogen: Gondwana Research, v. 61, p. 73–87, https://doi.org/10.1016/j.gr.2018.05.003.

Windley, B.F., Alexeiev, D., and Xiao, W., 2007, Tectonic models for accretion of the Central Asian Orogenic Belt: Journal of the Geological Society, v. 164, p. 31–47, https://doi.org/10.1144/0016-76492006-022.

Wolfram, L.C., Weinberg, R.F., Nebel, O., Hamza, K., Hasalová, P., Míková, J., and Becchio, R., 2019, A 60-Myr record of continental back-arc differentiation through cyclic melting: Nature Geoscience, v. 12, no. 3, p. 215–219, https://doi.org/10.1038/s41561-019-0298-6.

Xiao, W.J., Windley, B.F., Yuan, C., Sun, M., Han, C.M., Lin, S.F., Chen, H.L., Yan, Q.R., Liu, D.Y., Qin, K.Z., Li, J.L., and Sun, S., 2009, Paleozoic multiple subduction-accretion processes of the southern Altaids: American Journal of Science, v. 309, no. 3, p. 221–270, https://doi.org/10.2475/03.2009.02.

Xiao, W.J., Windley, B.F., Sun, S., Li, J., Huang, B., Han, C., Yuan, C., Sun, M., and Chen, H., 2015, A tale of amalgamation of three Permo-Triassic collage systems in Central Asia: Oroclines, sutures, and terminal accretion: Annual Review of Earth and Planetary Sciences, v. 43, no. 1, p. 477–507, https://doi.org/10.1146/annurev-earth-060614-105254.

Xu, J.F., Castillo, P.R., Chen, F.R., Niu, H.C., Yu, X.Y., and Zhen, Z.P., 2003, Geochemistry of late Paleozoic mafic igneous rocks from the Kuerti area, Xinjiang, northwest China: Implications for backarc mantle evolution: Chemical Geology, v. 193, no. 1–2, p. 137–154, https://doi.org/10.1016/S0009-2541(02)00265-6.

Yuan, C., Sun, M., Xiao, W., Li, X., Chen, H., Lin, S., Xia, X., and Long, X., 2007, Accretionary orogenesis of

the Chinese Altai: Insights from Paleozoic granitoids: Chemical Geology, v. 242, no. 1–2, p. 22–39, https://doi.org/10.1016/j.chemgeo.2007.02.013.

Žák, J., Verner, K., Holub, F.V., Kabele, P., Chlupáčová, M., and Halodová, P., 2012, Magmatic to solid state fabrics in syntectonic granitoids recording early Carboniferous orogenic collapse in the Bohemian Massif: Journal of Structural Geology, v. 36, p. 27–42, https://doi.org/10.1016/j.jsg.2011.12.011.

Závada, P., Schulmann, K., Konopásek, J., Ulrich, S., and Lexa, O., 2007, Extreme ductility of feldspar aggregates—Melt-enhanced grain boundary sliding and creep failure: Rheological implications for felsic lower crust: Journal of Geophysical Research. Solid Earth, v. 112, no. B10, https://doi.org/10.1029/2006jb004820.

Závada, P., Schulmann, K., Racek, M., Hasalová, P., Jeřábek, P., Weinberg, R.F., Štípská, P., and Roberts, A., 2018, Role of strain localization and melt flow on exhumation of deeply subducted continental crust: Lithosphere, v. 10, no. 2, p. 217–238, https://doi.org/10.1130/L666.1.

Zeng, Q.S., Chen, G., Wang, H., and Shan, Q., 2007, Geochemical characteristic, SHRIMP zircon U-Pb dating and tectonic implication for granitoids in Chonghuer basin, Altai, Xinjiang [in Chinese with English abstract]: Yanshi Xuebao, v. 23, no. 8, p. 1921–1932.

Zhang, C.L., Santosh, M., Zou, H.-B., Xu, Y.G., Zhou, G., Dong, Y.G., Ding, R.F., and Wang, H.Y., 2012, Revisiting the "Irtish tectonic belt": Implications for the Paleozoic tectonic evolution of the Altai orogeny: Journal of Asian Earth Sciences, v. 52, p. 117–133, https://doi.org/10.1016/j.jseaes.2012.02.016.

Zhang, C.L., Zou, H.B., Yao, C.Y., and Dong, Y.G., 2014, Origin of Permian gabbroic intrusions in the southern margin of the Altai Orogenic belt: A possible link to the Permian Tarim mantle plume?: Lithos, v. 204, p. 112–124, https://doi.org/10.1016/j.lithos.2014.05.019.

Zhang, J., Sun, M., Schulmann, K., Zhao, G., Wu, Q., Jiang, Y., Guy, A., and Wang, Y., 2015, Distinct deformational history of two contrasting tectonic domains in the Chinese Altai: Their significance in understanding accretionary orogenic process: Journal of Structural Geology, v. 73, p. 64–82, https://doi.org/10.1016/j.jsg.2015.02.007.

Zhang, J.H., Wang, J.B., and Ding, R.F., 2000, Characteristics and U-Pb ages of zircon in metavolcanics from the Kangbutiebao Formation in the Altay Orogen, Xinjiang [in Chinese with English abstract]: Regional Geology of China, v. 19, p. 281–287.

Zhang, P., Wang, G., Polat, A., Zhu, C., Shen, T., Chen, Y., Chen, C., Guo, J., Wu, G., and Liu, Y.T., 2018a, Emplacement of the ophiolitic mélanges in the west Karamay area: Implications for the Late Paleozoic tectonic evolution of West Junggar, northwestern China: Tectonophysics, v. 747, p. 259–280, https://doi.org/10.1016/j.tecto.2018.08.019.

Zhang, P., Wang, G., Polat, A., Shen, T., Chen, Y., Zhu, C., and Wu, G., 2018b, Geochemistry of mafic rocks and cherts in the Darbut and Karamay ophiolitic mélanges in West Junggar, northwestern China: Evidence for a Late Silurian to Devonian back-arc basin system: Tectonophysics, v. 745, p. 395–411, https://doi.org/10.1016/j.tecto.2018.08.018.

Zhang, Z.M., Zhao, G.C., Santosh, M., Wang, J.L., Dong, X., and Liou, J.G., 2010, Two stages of granulite facies metamorphism in the eastern Himalayan syntaxis, south Tibet: Petrology, zircon geochronology and implications for the subduction of Neo-Tethys and the Indian continent beneath Asia: Journal of Metamorphic Geology, v. 28, no. 7, p. 719–733, https://doi.org/10.1111/j.1525-1314.2010.00885.x.

Zhuang, Y., 1994, The pressure-temperature-space-time (P–T-S-t) evolution of metamorphism and development mechanism of the thermal-structural-gneiss domes in the Chinese Altaides: Acta Geologica Sinica, v. 7, no. 3, p. 267–281, https://doi.org/10.1111/j.1755-6724.1994.mp7003003.x.

Science Editor: Wenjiao Xiao
Associate Editor: Lu Wang

Manuscript Received 3 January 2020
Revised Manuscript Received 27 December 2020
Manuscript Accepted 26 January 2021

Printed in the USA